ACS Energy LETTERS

http://pubs.acs.org/journal/aelccp

REVIEW

Visualizing the Future: Recent Progress and Challenges on Advanced Imaging Characterization for All-Solid-State Batteries

Xia Zhang, Markus Osenberg, Ralf F. Ziesche, Zhenjiang Yu,* Julia Kowal, Kang Dong,* Yan Lu, and Ingo Manke*

Cite This: ACS Energy Lett. 2025, 10, 496−525

Read Online

ACCESS | Metrics & More | Article Recommendations

ABSTRACT: All-solid-state batteries (ASSBs) offer high safety and energy density, but their degradation and failure mechanisms remain poorly understood due to the buried interfaces within solid-state electrodes and electrolytes. Local probing methods are crucial for addressing key challenges such as interfacial instabilities, dendrite growth, and chemo-mechanical degradation. State-of-the-art imaging techniques provide critical insights into morphological, structural, and compositional evolution of the ubiquitous interfaces in ASSBs. This review highlights recent progress in cutting-edge visualization techniques, including neutron imaging, X-ray tomography, focused ion beam scanning electron microscopy, and cryogenic electron microscopy, which reveal microstructural and chemical changes in ASSBs at scales from the atomic to the macroscopic level. We particularly focus on the elusive failure behaviors at lithium anodes, composite cathodes, solid-state electrolytes, and beyond. Additionally, we discuss the strengths and limitations of each technique, aiming to enhance the understanding of ASSB operation and degradation mechanisms to advance the development of high-energy-density, high-safety ASSBs.

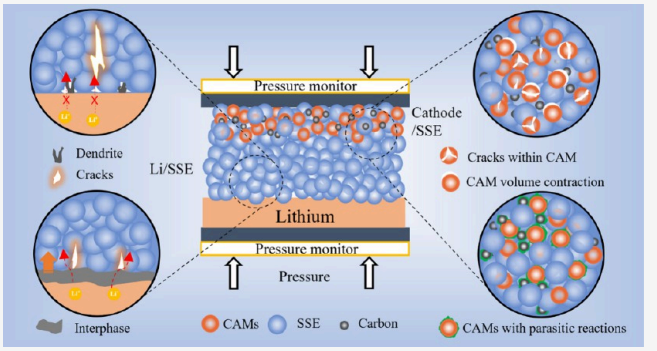

Over the past three decades, lithium-ion batteries (LIBs) have been instrumental in revolutionizing various aspects of our lives owing to their high flexibility and scalability.[1−5] However, as LIBs approach their theoretical energy density limit of approximately 300 Wh kg^{-1} due to the performance limitations of battery materials ($LiCoO_2$, $LiMn_2O_4$, $LiFePO_4$, graphite, etc.), they are unable to meet the ever-increasing demands (e.g., for the long-range required by electric vehicles), which now exceeds 500 Wh kg^{-1}.[6−9] Additionally, the use of a liquid electrolyte containing flammable organic solvents (diethyl carbonate, ethylene carbonate, ethyl methyl carbonate, etc.) in LIBs poses a significant safety risk, with incidents of fire or explosion not uncommon.[8]

In contrast, all-solid-state batteries (ASSBs), employing solid-state electrolytes (SSEs) instead of organic liquid electrolytes (LEs), hold the promise of higher energy densities in the case of using lithium anode while also addressing safety concerns such as flammability and electrolyte leakage. However, in practical applications, ASSBs generally suffer from rapid capacity decay, higher polarization, and poor cycling capacity. This is mainly caused by the widespread interfacial issues compared to LE-based batteries.[10−12] Specifically, factors such as grain boundaries, loose physical contacts, and (electro-)chemical reactions contribute to increased resistance at interfaces/interphases of anode−electrolyte (Li/SSE), cathode−electrolyte (cathode/SSE), and cathode active materials−electrolyte (CAMs/SSE), hindering the charge (electron and ion) transfer.[13,14] Moreover, while rigid SSEs are less resistant to stress originating from solid electrodes compared to flowable LEs, the accumulation of mechanical stresses within ASSBs upon long cycling results in crack propagation.[15−17] These cracks significantly impair the cycling performance of ASSBs by obstructing electron and ion conduction pathways. Hence, a comprehensive understanding of the intricate Li/SSE interfacial

Received: September 6, 2024
Revised: October 22, 2024
Accepted: December 12, 2024
Published: December 27, 2024

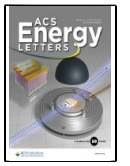

degradation and ionic diffusion behavior in SSEs at the micro/nano-scale is imperative to enhance ASSB performance.[18,19]

However, interpreting interfacial reactions and failure mechanisms in ASSBs poses significant challenges due to the complicated electro-chemo-mechanical interplay ranging from the atomic to micrometer and cell levels. Moreover, conventional characterization methods often struggle to detect the buried interface within ASSBs, and cell disassembly can destroy the integrity of the interfaces, making the results inaccurate.[20] Additionally, revealing the kinetics of electrochemical reactions in ASSBs requires a comprehensive understanding that spans the fields of electrochemistry, materials science, and mechanics. The presence of ubiquitous interfaces within ASSBs further complicates the characterization and understanding of these intricate reactions. Thus, a multidisciplinary approach is essential to elucidating the underlying mechanisms governing the electrochemical processes in these advanced energy storage systems. Particularly, advanced visualization tools hold significant promise for facilitating the observation of internal structural evolution within sealed cells. (1) Neutron imaging (NI) has emerged as a powerful technique for characterizing ASSBs, offering distinct advantages due to the high penetration depth of neutrons and their sensitivity to light elements, such as lithium (Li). This nondestructive method allows for the examination of bulk solid electrodes and the internal distribution of Li within cells, providing critical insights into phenomena such as Li stripping/plating, Li dendrite formation, and Li dynamics under the different states of charge within ASSBs. Notably, neutron tomography can generate three-dimensional (3D) images, thereby revealing the internal structure and identifying potential defects or degradation processes within the battery.[21] (2) In

Collectively, sophisticated imaging methodologies enable researchers to gain profound insights into the dynamic processes occurring at multiple scales, thereby enhancing understanding of the fundamental mechanisms governing the various ASSBs systems. The capacity to visualize internal changes is pivotal for advancing the design and optimization of energy storage technologies.

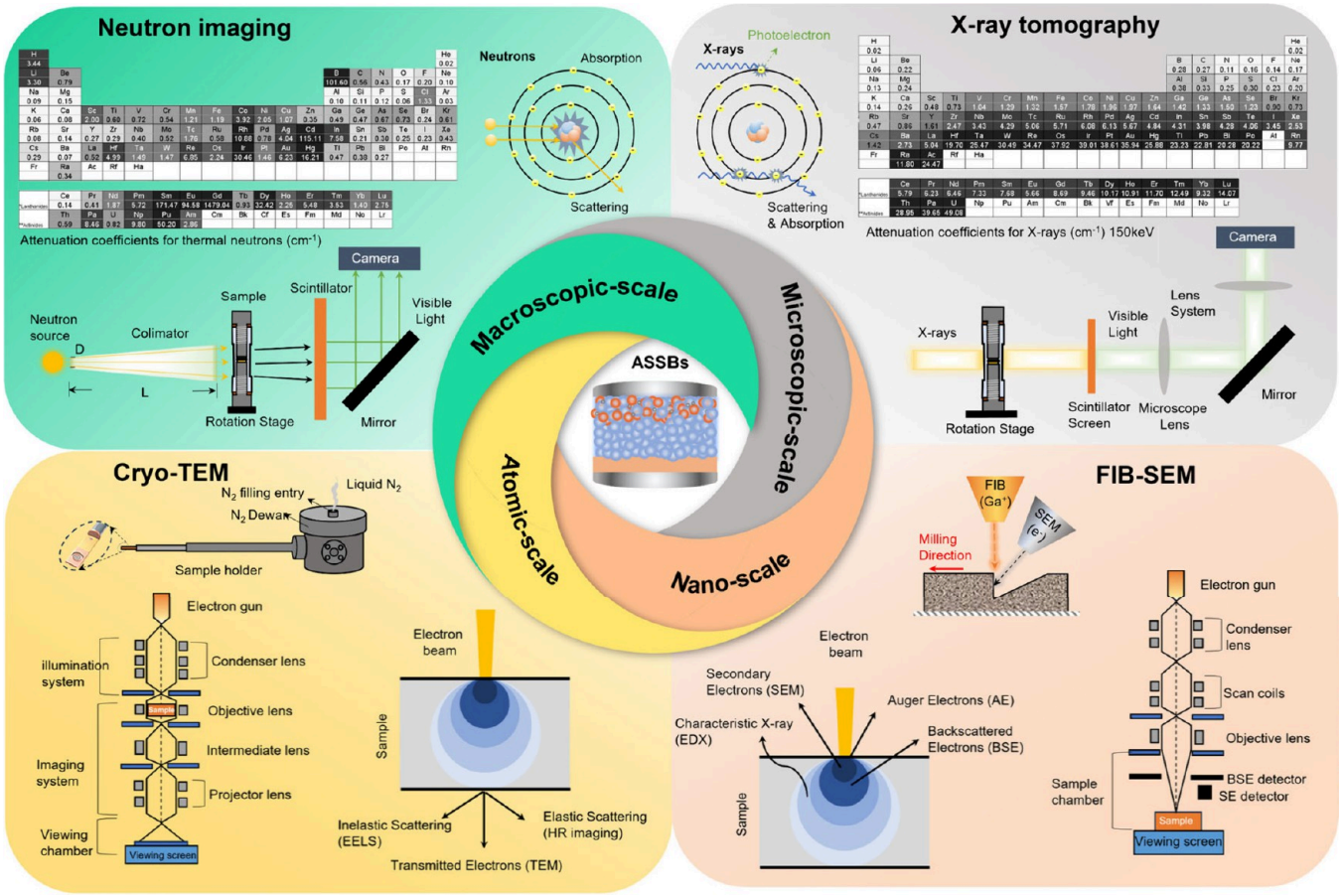

Figure 1. Schematic representation of imaging characterization principles. The techniques are presented in descending order of resolution. Top left includes thermal neutron interactions with nuclei, and their attenuation is independent of the atomic number across the periodic table; the neutron beamline station setup is also presented. Top right features X-ray interactions with outer electron shells (for 150 kV X-ray), which produce an increasing attenuation coefficient with the atomic number in the periodic table, and a schematic demonstration of a synchrotron X-ray tomographic beamline station. Bottom right shows the working principle of the FIB-SEM and the related interactions of the incident electron-beam to the specimen. Bottom left includes the cryo-TEM sample transfer holder, a schematic of TEM working principles, and associated electron-beam interactions with matter.

https://doi.org/10.1021/acsenergylett.4c02476
ACS Energy Lett. 2025, 10, 496−525

addition, synchrotron X-ray tomography (XRT), made possible by advancements in synchrotron light sources, facilitates high-resolution characterization of ASSB components and enables real-time monitoring of interface evolution under *operando* or *in situ* conditions. This technique elucidates how electrochemical processes impact individual cell components in real-time operational scenarios. The high penetration capabilities of synchrotron X-rays are essential for nondestructively detecting internal structures, particularly in tomography, where 3D information is acquired as the sample rotates.[22,23] (3) Furthermore, advanced electron-based imaging techniques, such as focused ion beam scanning electron microscopy (FIB-SEM) and cryogenic electron transmission microscopy (cryo-TEM), provide complementary insights into structural interface evolution from atomic to nanoscale and offer quantitative information on changes in chemical composition.[24−29] Collectively, these sophisticated imaging methodologies enable researchers to gain profound insights into the dynamic processes occurring at multiple scales, thereby enhancing our understanding of the fundamental mechanisms governing the various ASSBs systems. The capacity to visualize internal changes is pivotal for advancing the design and optimization of energy storage technologies.

In this review, we highlight the fundamental principles, advancements, and developments of state-of-the-art imaging techniques, including NI, XRT, FIB-SEM, and cryo-TEM, employed in ASSBs across multiscale spatial resolution. These imaging methods are expected to elucidate charge transport behaviors and short-circuit failure mechanisms at the anode/SSE interface and at the cathode/SSE interface. Such insights can be correlated to electrochemical performance, thereby enhancing our understanding of the working and degradation mechanisms of ASSBs. Additionally, we provide a comprehensive summary and discussion of the advantages and limitations of emerging imaging techniques. We expect that these discussions will enrich researchers' perspectives, deepen the understanding of the operational mechanisms of ASSBs, foster interdisciplinary interest among scientists, and inspire innovative solutions to the challenges currently facing ASSB technologies.

FUNDAMENTALS OF ADVANCED IMAGING TECHNIQUES

Understanding the mechanisms that govern interface ion transport, electrode microstructure formation, and electrochemical kinetics across multiple scales—atomic, nanometric, microscopic, and macroscopic—is critical for the development of high-performance ASSBs. Advanced imaging techniques facilitate intuitive investigations with multiscale spatial resolution, enabling precise monitoring of internal electrochemical reaction processes in ASSBs. However, the implementation of these techniques in ASSBs remains in its early stages. Consequently, a thorough understanding of advanced imaging methods is essential for advancing the characterization of ASSBs. This section reviews the imaging fundamentals, operational workflows, advantages, and future challenges of various advanced neutron-, X-ray-, and electron-based imaging techniques, organized by imaging resolution from large to small (i.e., from millimeter to atomic scale), as summarized in Figure 1.

Understanding the mechanisms that govern interface ion transport, electrode microstructure formation, and electrochemical kinetics across multiple scales—atomic, nanometric, microscopic, and macroscopic—is critical for the development of high-performance ASSBs.

FUNDAMENTALS OF NEUTRON IMAGING

Interaction of Neutrons with Matter. Neutrons, being electrically neutral, interact with matter primarily through nuclear interactions rather than electromagnetic forces. Their behavior in matter depends on their energy, ranging from cold to thermal neutrons (~meV to eV).[30] Unlike charged particles, neutrons primarily interact through nuclear forces, making them less likely to interact with matter and more capable of deep penetration. As a result, the interaction of neutrons with various elements differs significantly across the periodic table (Figure 1, top left) and can vary considerably between isotopes of the same element.[31] When neutrons collide with atomic nuclei, they can scatter (either elastically or inelastically) or be absorbed, triggering nuclear reactions. In elastic scattering, neutrons rebound off the nucleus without energy transfer, whereas inelastic scattering involves energy transfer that excites the nucleus. Absorption events may lead to nuclear fission, activation (making the nucleus radioactive), or the emission of particles like protons or alpha particles.[32] The likelihood of these interactions is quantified by the neutron cross-section, which varies depending on the neutron energy and the target material.

Given that atomic nuclei are much smaller than their electron shells, neutron absorption is relatively weak in many common materials. This property enables neutrons to penetrate several millimeters to centimeters into metal layers, making them an effective probe for examining electrode materials in equipment that controls pressure, temperature, and other conditions.[32] Additionally, neutrons are highly sensitive to light elements such as hydrogen (H) and Li, providing exceptional potential for the spatially resolved detection of these elements in bulk components of ASSBs. Furthermore, the sensitivity of neutrons to light elements can be enhanced or reduced by selectively enriching or depleting certain isotopes. Isotopes of the same element—sharing the same number of protons but differing in neutron count—exhibit distinct neutron scattering and absorption characteristics.[33] For instance, the two primary isotopes of Li, ^{6}Li and ^{7}Li, exhibit significant differences in neutron absorption coefficients, as ^{6}Li has a much larger absorption cross section than ^{7}Li. This characteristic can be leveraged to investigate the Li diffusion process in Li solid-state batteries by detecting the movement of ^{6}Li or ^{7}Li.[31]

Neutron Imaging. Neutron imaging (NI), pioneered by Kallman and Kuhn in 1935 in Germany, is a noninvasive method for investigating the bulk structural information within the batteries. Specifically, neutron imaging encompasses neutron radiography, which captures two-dimensional (2D) images, and neutron tomography, which can visualize 3D volumes, both offering nondestructive insights into the dynamic electrode evolution through *operando* and *in situ* methods. Conventional neutron attenuation radiography involves transmitting a collimated beam of thermal neutrons (wavelengths approx-

https://doi.org/10.1021/acsenergylett.4c02476
ACS Energy Lett. 2025, 10, 496−525

imately 1.0−2.5 Å) or cold neutrons (wavelengths greater than 2.5 Å) through a sample and capturing the attenuated beam with a position-sensitive detector, as illustrated in Figure 1 (top left).[34] According to the Lambert−Beer law (detailed explanation in next section), the ratio of transmitted to incident beam intensity is an exponential function of the thickness attenuation coefficient of the sample for a given neutron energy. In neutron tomography, the sample is incrementally rotated around a fixed, usually vertical, axis within the beam. A position-sensitive detector captured a projection image at each angular increment. A set of projections spanning an angular range of 180° or 360° is used as input for mathematical reconstruction, typically employing the back projection algorithm, to determine the 3D distribution of attenuation coefficients within the sample volume.[34] NI has been recognized as a direct and effective method for assessing Li-ion transport,[35] spatial distribution,[36] and concentration changes[37] during cell cycling, largely due to its deep penetration and sensitivity to Li. These capabilities are crucial for optimizing the battery performance. However, its application in ASSBs remains in its early stages due to limited global access to neutron-related techniques and moderate spatial resolution of around 10 μm.[30] Overcoming the resolution limitations of neutron imaging is challenging because it requires intense radiation sources to produce sufficient signal per pixel. Neutron sources, however, are typically up to 4 orders of magnitude less intense than synchrotron radiation sources, making it unlikely for neutron imaging to attain the resolution levels of X-ray imaging. As a result, X-ray tomography, with its ability to achieve resolutions down to 1 μm, has rapidly become a complementary technique to NI. In the following section, the advancements of X-ray tomography techniques are summarized, emphasizing their role in broadening the scope of imaging methods for battery research.[34]

FUNDAMENTALS OF SYNCHROTRON X-RAY TOMOGRAPHY

Interaction of Synchrotron X-rays with Matter. Synchrotron X-rays are a form of electromagnetic radiation with high energy and short wavelengths, typically in the range of 0.01 to 10 nm. Unlike neutrons, X-rays primarily interact with the outer electron shells of the atoms, providing excellent contrast for heavy elements and high-resolution imaging. When a parallel beam of X-rays passes through a medium, it interacts with the material in a variety of ways, mainly by absorption, scattering, and transmission. Specifically, (1) denser materials or those with higher atomic numbers absorb more X-rays. This occurs because these materials have more electrons that can interact with the X-rays, resulting in higher absorption. Therefore, the absorption of X-rays by an element in the periodic table increases proportionally with its atomic number, as demonstrated in Figure 1 (top right). The absorbed X-rays do not pass through the material, creating contrast in the resulting image based on the varying densities and compositions of the materials. (2) Scattering happens when X-rays change direction upon colliding with electrons in the material. This interaction causes the X-rays to deviate from their original path, leading to a decrease in image clarity. Similar to neutrons, scattering can be further categorized into coherent (elastic) scattering, where the energy of X-ray remains the same, and incoherent (inelastic) scattering, where the X-ray loses energy. (3) Transmission refers to the X-rays that are neither absorbed nor scattered and continue to pass through the object. The extent of transmission depends on the density, atomic number, and thickness of the sample. Materials with lower density, lower atomic numbers, and thinner structures allow more X-rays to transmit through them, resulting in lighter areas on the X-ray imaging projections.

Synchrotron X-ray tomography, which we will focus on here, is a 3D imaging technique usually based on the absorption characteristics of different materials to X-rays. A detailed elucidation of the interaction mechanism of the X-rays with the sample material is essential before the principle of X-ray tomography is presented. The intensity and phase variations of an electromagnetic X-ray wave as it travels through an object vary with the complex refractive index, n:

$$n = (1 - \delta) + i\beta \tag{1}$$

Here, the real part (δ) is the refractive decrement indicating the phase shift as the X-ray propagates through the materials, while the imaginary part (β) is the attenuation (absorption) part of n related to the linear absorption coefficient μ by

$$\mu = \frac{4\pi}{\lambda}\beta \tag{2}$$

Here, λ represents the X-ray wavelength. From eq 2, X-ray attenuation coefficients vary for different materials with different β-values. The δ-value for various materials represents the degree of phase shift of the incident X-rays. Given these two different attenuation mechanisms of X-rays traveling through the material, the attenuation contrast and phase contrast of different materials can be employed for synchrotron X-ray tomography. Specifically, attenuation contrast tomography reveals the internal structure of a material by measuring variations in X-ray absorption related to density and composition. In contrast, phase contrast tomography improves image resolution by detecting shifts in the phase of X-rays as they traverse the material, making it especially effective for capturing fine details in low-density or soft materials.

Attenuation Contrast Tomography. As the X-rays traverse the sample mounted on the rotation stage (a typical beamline station shown in Figure 1 (top right)), the attenuated X-ray beam is captured at different angles by the detector system. Within the detector, a scintillator converts the X-rays to visible light, which is then projected onto a detector. This detector reads out the projection image for further digital processing by a computer. The intensity I of an X-ray beam after passing through an object of thickness d, characterized by the linear X-ray attenuation coefficient μ, is described by the Beer−Lambert Law (also applies to neutron beam):

$$I = I_0 e^{-\int_0^d \mu dx} \tag{3}$$

where I_0 is the intensity of the incident X-ray beam, I is the intensity of the transmitted X-ray beam, μdx is the linear attenuation coefficient which varies with the density of material and the energy of X-ray, and $\int \mu dx$ is the integral of the attenuation coefficient along the path of the X-ray beam through the object. In attenuation contrast tomography, the main interaction between X-rays and the sample is absorption. When no absorption edge is present at the X-ray energy of interest (E), the imaginary part of the refractive index, β, can be represented as indicated in eq 4:

$$\beta = \frac{h^4 c^4}{2\pi}\rho_e \frac{z^3}{E^4}\left(\frac{1}{m}\right) \tag{4}$$

Here, h is the Planck constant, c is the speed of light, ρ_e is the sample's electron density, and Z is the atomic number of

https://doi.org/10.1021/acsenergylett.4c02476
ACS Energy Lett. 2025, 10, 496−525

materials. According to eq 4, β is proportional to the cube of the atomic number (Z^3). Consequently, for materials composed of heavy elements, image contrast mainly arises from the variations in β values between phases. The difference in contrast between the two phases is given by $\Delta\beta = \beta_1 - \beta_2$.

Phase Contrast Tomography. Conversely, for phases with light elements and low atomic numbers (such as H or Li), attenuation contrast tomography is ineffective in distinguishing different components. In these situations, phase contrast tomography is a more suitable technique. The real part of the refractive index, δ, can be described by eq 5:

$$\delta = \frac{h^2 e^2}{8\pi^2 \varepsilon_0 m_e} \rho_e \frac{1}{E^2} \tag{5}$$

In this equation, ε_0 represents the vacuum dielectric constant and m_e is the electron mass. This indicates that δ is independent of atomic number Z, with the difference between phases given by $\Delta\delta = \delta_1 - \delta_2$. For light elements, the variation in δ between materials is several orders of magnitude greater than that in β. Consequently, phase contrast tomography can significantly enhance the image contrast of samples containing light elements, such as Li or carbon.

Data Acquisition and Measurement Workflow. Achieving high-quality synchrotron XRT data requires careful consideration of critical factors, such as sample requirements and beamline equipment parameters. The following workflow is recommended before conducting synchrotron X-ray tomographic measurements. This workflow also applies to the measurement and acquisition of neutron imaging data, and the detailed process is presented as an example of a synchrotron X-ray tomography measurement.

Sample Size and Fields of View. Selecting the appropriate sample size and field of view (FOV) is crucial for balancing spatial resolution, transmission, and therefore possible image contrast with the region of interest (ROI). The sample size must be compatible with the beamline setup to ensure the optimal imaging. For high-resolution scans with a spatial resolution below 1 μm, smaller samples, typically a few millimeters in size, are preferred for detailed imaging of microstructures. Conversely, larger samples may be necessary when examining the overall architecture of components such as ASSBs and pouch cells. In micro-XRT and nano-XRT systems, the FOV is generally on a micrometer to millimeter scale, allowing for high-resolution imaging. For larger samples, if a ROI region exceeds the FOV, stitching techniques can be employed to combine multiple scans into a comprehensive data set.

Compatibility with In Situ Devices and Beamline Facilities. Tomographic measurements can be conducted in three modes: *ex situ*, *in situ*, and *operando*, depending on experimental expectations:

(a) For *ex situ* measurements, a single scan test is performed for each cell by scanning multiple cells at specific electrochemical states.
(b) *In situ* testing involves performing multiple scans of the same cell at different cycle states, enabling detailed examination of changes over time without disassembling the cell.
(c) *Operando* measurements provide real-time monitoring of a cell while it is operational, capturing dynamic phase and structural changes during electrochemical reactions.

Operando testing, while incredibly informative, also poses significant challenges. The high cost of trial-and-error means that any interruption, such as instability of the *in situ* cell setup or failure of the equipment on the beamline, can lead to premature suspension of the cell cycling process. Such interruptions may prevent the collection of complete and useful data, highlighting the importance of stable and reliable *in situ* equipment and setups. While it is challenging to establish a functional and stable setup/cell on sufficiently small scales to enable microstructure imaging, a few types of tomographic cells have been designed and have been shown to be effective and practical in tomographic measurements.[38−40] Such a design needs to be further optimized for different research systems, especially ASSBs as required.

Determination and Consideration of Measurement Parameters. The energy and brilliance of the incident X-rays must be carefully selected based on the absorption characteristics of the sample. For ASSBs, typical energy ranges from 5 to 100 keV are used. Higher-energy X-rays can penetrate thicker samples and denser materials but may result in reduced contrast. A transmission value of approximately 30% is optimal for obtaining projection images with good attenuation contrast and desirable results for battery samples.[41] After determining the X-ray energy, the beam brilliance—defined as the number of photons per second within 0.1% of the central wavelength bandwidth, factoring in angular divergence, beam cross-sectional area, and the camera configuration—highly impacts the exposure time needed to achieve a satisfactory signal-to-noise ratio and overall acquisition time. Longer exposure times and a higher number of projections can enhance the image quality but increase the acquisition time. Temporal resolution is the third critical factor for tomographic imaging. The scan time, influenced by exposure time and the number of projections, must be short enough to capture dynamics accurately for *in situ* and *operando* measurements. However, a higher temporal resolution can result in increased image noise.

Data Reconstruction and Postprocessing. Upon completing the tomographic measurement, accurate reconstruction and meticulous postprocessing are essential for extracting meaningful information from the imaging data. Commonly used algorithms, such as filtered back projection (FBP) and iterative reconstruction, convert the 2D projections into 3D volumetric data. Iterative reconstruction methods often deliver superior image quality by minimizing noise and reducing artifacts. It is crucial to detect and correct common issues such as ring artifacts and noise to preserve data integrity. Once the 3D volume is reconstructed, the segmentation process is carried out to distinguish and separate various regions, phases, or components within the sample. This step is especially significant in imaging ASSBs, as it allows for the extraction of key features, such as porosity, grain boundaries, cracks, voids, and other defects or signs of degradation. Following segmentation, quantitative analysis is conducted to derive specific characteristics describing the evolution of internal microstructures, including particle size and distribution, crack propagation, interfacial properties, etc. These extracted characteristics are then correlated with SSB performance to provide insights into the working and degradation mechanisms and to guide high-performance SSB design.

Overall, by carefully considering sample size, FOV, *operando*/*in situ* device compatibility, measurement parameters, and data processing techniques, researchers can maximize the potential of synchrotron X-ray tomography. Ongoing advancements in this field will continue to enhance its application in ASSB research,

https://doi.org/10.1021/acsenergylett.4c02476
ACS Energy Lett. 2025, 10, 496−525

offering deeper understanding and innovative solutions for material characterization.

FUNDAMENTALS OF ELECTRON-BASED IMAGING

Electron-beam imaging techniques play a pivotal role in advancing the understanding of ASSBs at the nanoscale. ASSBs are characterized by solid−solid interfaces between the solid electrolyte, electrodes, and interlayers, where intricate mechanical, chemical, and electrochemical reactions occur. These interfaces, ranging from the atomic scale to a few nanometers, fall below the resolution limits of X-ray tomography, which typically resolves features in the hundreds of nanometers range.

Due to high-resolution 3D imaging capacities, the FIB-SEM tomography technique has been effectively utilized to examine the interface contact, void formation, crack propagation, and dendrite growth within ASSBs. Cryo-TEM, on the other hand, provides atomic-scale insights into the evolution of solid-electrolyte interphase (SEI), defect formation, and grain boundaries (GB) diffusion inside ASSBs. This section explores the fundamentals of these two advanced electron imaging techniques, FIB-SEM and cryo-TEM, along with their operational workflows to foster a deeper understanding of the fine structures within ASSBs.

Interaction of Electron Beam with Matter. The electron beam used in electron microscopy is generated in an electron gun, typically using either a thermionic source, such as a tungsten filament, or a field emission source. The electrons are then accelerated by high voltage, ranging from kilovolts (kV) to several hundred kV, and focused through electromagnetic lenses, as displayed in Figure 1 (bottom right). When the accelerated electron beam interacts with matter, a variety of electrostatic (Coulomb) interactions occur, generating signals that provide critical information about the surface morphology, composition, and structure of the sample. These interactions, as illustrated in Figure 1 (bottom right), are broadly categorized into elastic and inelastic scattering. Elastic scattering results primarily in the emission of backscattered electrons (BSEs) and the formation of diffraction patterns, both crucial for compositional contrast and crystallographic analysis. In contrast, inelastic scattering produces secondary electrons (SEs), characteristic X-rays, and Auger electrons, which are commonly used for surface imaging, elemental analysis, and spectroscopy.

These electron microscopy techniques exploit these interactions to provide detailed insights into solid electrode materials at nano- to atomic scales, making them invaluable tools that complement neutron and X-ray imaging. As charged particles, electrons interact more intensely with matter compared with neutrons and X-rays, resulting in a shallower penetration depth and enhanced contrast across various imaging modes. As a result, when transmission imaging is required, the samples must be exceptionally thin to allow electrons to pass through.

FUNDAMENTALS OF FIB-SEM TOMOGRAPHY AND OPERATIONAL WORKFLOW

Fundamentals of FIB-SEM Tomography. FIB-SEM tomography is a dual-beam technique that combines two powerful functionalities: a focused ion beam (FIB) for sample modification and milling and scanning electron microscopy (SEM) for high-resolution imaging. The FIB system employs heavy ions (typically gallium) to precisely mill or sputter thin layers from the sample. This controlled layer-by-layer removal is essential for revealing subsurface structures. After each layer is removed, the SEM captures a high-resolution image of the newly exposed surface. The SEM operates by scanning the surface with a focused electron beam, generating signals such as SE and BSE, as shown in Figure 1 (bottom right). These signals are pivotal for producing high-resolution images and extracting the compositional information. The resolution achievable in SEM can be estimated using the Rayleigh criterion:

$$d = \frac{0.61\lambda}{\mathrm{NA}} \tag{6}$$

where d is the resolution, λ is the wavelength of the electron beam, and NA is the numerical aperture of the lens system. This formula underscores the dependence of resolution on both the electron wavelength and the optical capabilities of the system. The integration of FIB and SEM enables simultaneous imaging, milling, and material modification, making this technique particularly useful for high-resolution 3D imaging, site-specific sample preparation, and microstructural analysis in fields, such as materials science and ASSB research.

FIB-SEM Sample Preparation. Sample preparation for FIB-SEM is a critical step that directly impacts the quality of both imaging and analysis. Proper preparation ensures that samples can be imaged and processed without significant damage or artifacts, allowing for a detailed analysis of microstructures, interfaces, and defects in ASSBs. Several parameters must be considered before ion beam milling, including sample sensitivity to ion beam damage, sample conductivity, and vacuum compatibility. For instance, samples from ASSBs, particularly those at the interface of the Li anode and SSEs, are highly sensitive to ion beam damage. In such cases, low ion energies must be used to preserve the structural integrity of the sample. Sample preparation should also occur under vacuum conditions, as exposure to air can lead to dehydration or other structural changes, potentially affecting the properties of the material. Additionally, nonconductive samples can accumulate charge during SEM imaging. To mitigate this, a conductive layer (such as carbon or gold) is often sputtered onto the sample before measurement.

FIB-SEM Sample Transferring. Transferring samples between milling and imaging stages in FIB-SEM is straightforward because the entire process occurs within a vacuum chamber. However, precautions must be taken to avoid contamination and ensure proper alignment when switching between ion beam milling and SEM imaging. Sample holders and stages are designed for easy access to both beams, enabling precise control over sample orientation and movement during the milling and imaging processes.

FIB-SEM Sample Imaging and Data Analysis. FIB-SEM offers high-resolution imaging of surface topographies and cross sections through the SEM component. SE imaging provides a detailed surface morphology, while BSE allows for compositional contrast. By repeating the milling process iteratively, a series of 2D images is produced. These images are then aligned and reconstructed into a 3D visualization using specialized software such as Amira, ImageJ/Fiji, and MATLAB, among others. The alignment and reconstruction process is powered by advanced algorithms, often based on principles such as Fourier transforms, which manipulate spatial frequency components to enhance the accuracy of the 3D reconstruction. These algorithms ensure that the resulting 3D model accurately reflects the internal structure of the sample.

https://doi.org/10.1021/acsenergylett.4c02476
ACS Energy Lett. 2025, 10, 496−525

From these 3D reconstructions, quantitative metrics such as the pore size distribution, GB characteristics, and phase distribution can be extracted. Such analyses are critical for understanding failure mechanisms and optimizing materials in ASSBs. The capability of FIB-SEM to visualize complex structures at tens-of-nanometer resolution fills the gap between XRT and TEM, making it an invaluable tool for advanced materials research and analysis.

FUNDAMENTALS OF CRYO-TEM AND OPERATIONAL WORKFLOW

Fundamentals of Cryo-TEM. Cryo-TEM is a specialized form of TEM that allows high-resolution imaging by transmitting an electron beam through a frozen, hydrated sample.[42−44] The imaging can be performed in either bright-field mode, where transmitted electrons are detected, or dark-field mode, which captures scattered electrons (as illustrated in Figure 1, bottom left). Cryo-TEM is particularly valuable for investigating beam-sensitive materials, such as Li deposition, SEI, cathode-electrolyte interphase (CEI), and other thermally unstable components within ASSBs. By preserving samples in their native, frozen-hydrated state, cryo-TEM avoids artifacts caused by dehydration or chemical fixation, allowing researchers to study delicate structures without compromising their integrity.

Cryo-TEM Sample Preparation. Vitrification is a critical step in cryo-TEM sample preparation, as it ensures that the sample is frozen rapidly enough to prevent the formation of ice crystals, which could damage delicate structures and obscure fine details. By freezing the sample into an amorphous, glass-like state, vitrification preserves the native structure of materials for high-resolution imaging. Once vitrified, the sample is mounted onto a specialized cryo-TEM grid, which holds the ultrathin sample sections during imaging.

Sample thickness is crucial for cryo-TEM, as the electron beam must pass through the sample to form high-quality images. Typically, the sample must be less than 100 nm thick. For solid-state battery materials, FIB-SEM can be employed to prepare ultrathin lamellae, ensuring that the samples are suitable for cryo-TEM analysis. Additionally, an innovative approach integrates the TEM grid as part of the current collector of batteries, enabling the direct plating of Li onto the grid for more accurate studies of electrode stripping and plating behavior during cycling. Careful handling is essential, particularly for sensitive battery electrolytes, to prevent alteration of the structure during preparation.

Cryo-TEM Sample Transferring. Transferring cryo-TEM samples is more challenging than conventional TEM due to the need to maintain cryogenic temperatures throughout the process. After vitrification, samples are transferred into the cryo-TEM using specialized cryoholders (as shown in Figure 1, bottom left), which keep the sample at liquid nitrogen temperatures (about −196 °C). This temperature is necessary to prevent ice recrystallization and maintain the structural integrity of the sample. The transfer process must be carefully controlled to avoid any exposure to air or moisture, which could lead to contamination or structural compromise.

Cryo-TEM Imaging and Data Analysis. Cryo-TEM offers similar capabilities to conventional TEM, with additional advantages for materials that are sensitive to a beam. The technique allows the acquisition of data on morphology, crystalline structure (using high-resolution transmission electron microscopy (HRTEM)), elemental distribution (through energy-dispersive spectroscopy (EDS)), and electronic structure (via electron energy loss spectroscopy (EELS)).[45,46] Importantly, cryo-TEM minimizes artifacts, making it ideal for analyzing sensitive materials, particularly for battery components. Image contrast in cryo-TEM is derived from variations in electron scattering that reflect differences in the sample density, thickness, and composition. Since samples are highly susceptible to radiation damage, low-dose imaging is crucial. Phase contrast is a key technique used to enhance visibility in low-contrast samples. By leveraging the phase shifts of electron waves caused by differences in sample thickness and density, we can reveal subtle structural details. Techniques such as defocusing the objective lens or using phase plates allow researchers to exploit these phase differences, enhancing the visualization of features that would otherwise remain indistinguishable.

The interpretation of cryo-TEM data involves sophisticated analytical processes to elucidate complex sample structures. Due to the low-dose imaging conditions, acquired images are inherently noisy and require rigorous processing. Techniques such as noise reduction, contrast enhancement, and filtering are applied to improve image clarity and fidelity. For samples requiring 3D insights, cryo-TEM tomography is employed. This involves capturing a series of 2D images commonly using a tilt range of at least ±60°, which are computationally reconstructed into a 3D volume. This reconstruction enables a detailed examination of molecular and atomic architectures. Advanced software tools such as IMOD, RELION, EMAN2, et al. facilitate the analysis of these 3D structures, providing critical insights into the organization and interactions within battery interfaces, ultimately advancing our understanding of their working mechanisms.

COMPARISON OF THREE IMAGING MODES

Neutrons, X-rays, and electrons interact with matter in distinct ways. By comparison of the mass attenuation coefficients of various elements for neutrons and X-rays, the following conclusions can be made:

(a) Neutrons exhibit high sensitivity to certain light elements. These elements absorb X-rays weakly and therefore provide poor contrast in X-ray imaging but offer excellent contrast in neutron imaging.

(b) Neutron attenuation coefficients are not strongly dependent on atomic number. This character facilitates contrast discrimination between neighboring elements. In contrast, X-rays display similar absorption characteristics for neighboring elements with increasing atomic number, such as aluminum/silicon (Al/Si) or manganese/iron (Mn/Fe).

(c) Neutrons can usually penetrate thicker layers of metals such as Fe, copper (Cu) and lead (Pb), which cannot be penetrated by standard X-ray imaging equipment at energies of hundreds of keV.

(d) Neutrons can distinguish between isotopes, such as protium/deuterium ($^{1}H/^{2}H$) or lithium-6/lithium-7 ($^{6}Li/^{7}Li$), a capability that X-rays lack.

The main differences between neutron, X-ray, and electron imaging modes are summarized in Table 1. The variations in interaction strength explain why electrons are ideal for imaging thin samples with the highest resolution, neutrons are suited for thicker samples at lower resolutions, and X-rays occupy an intermediate position. The unique interaction of neutrons is

https://doi.org/10.1021/acsenergylett.4c02476
ACS Energy Lett. 2025, 10, 496−525

Table 1. Main Characteristics of the Interaction between Neutrons, X-rays, and Electrons with Solid Matter

	Neutrons (thermal)	X-rays (100 keV)	Electrons (100 keV)
Interaction principle	Nuclear: nuclei Magnetic: electrons	Electromagnetic with electrons	Coulomb with electrons and nuclei
Function $\mu(Z)$	Irregular	Regular	Regular
Sensitivity to low Z	Yes	No	No
Interaction of strength	Weak	Medium	Very strong
Detection depth	Centimeters	Millimeters	Nanometers
Typical sample thickness	10−500 mm	1−10 mm	10−100 nm

particularly beneficial for imaging light elements and magnetic structures.

Despite the power of modern imaging technologies, each modality has intrinsic limitations that researchers continue to address. In the case of NI, the primary challenge has traditionally been its lower spatial resolution compared to those of other imaging techniques. Recent innovations, however, have mitigated these issues. The development of novel neutron detectors, employing improved scintillation materials and advanced semiconductor technologies, has enhanced the spatial resolution. These detectors are more efficient at capturing neutron interactions, significantly reducing noise, and providing clearer, more detailed images. For XRT, challenges remain in noninvasively capturing the rapid dynamics processes that occur during the operation of ASSBs. Critical electrochemical phenomena such as the Li dendrite nucleation, crack propagation, and hard short circuits within ASSBs often occur on very short time scales, usually requiring subsecond temporal resolution for accurate observation. Achieving this level of temporal resolution is complicated by the trade-offs between spatial resolution and image quality. Faster imaging typically necessitates a higher X-ray flux, which can introduce noise and degrade the quality of the reconstructed images. However, the development of high-brightness synchrotron sources and advances in semiconductor-based X-ray detector technology have substantially enhanced temporal resolution. These detectors capture finer details by minimizing noise and improving the photon detection efficiency.

In FIB-SEM, mitigating sample damage during measurement remains a major challenge. Traditional Ga ion sources, commonly employed for material milling, can induce amorphization, implantation of ions, or localized heating, altering the native structure of sensitive battery materials. This issue is particularly acute when studying Li metal, sulfides, or other sensitive materials, as their chemical and structural integrity is critical to understanding their behavior in real electrochemical conditions. Moreover, the limited volume of material accessible to conventional FIB-SEM systems restricts their utility for large-scale investigations. For instance, in thick electrode layers used in next-generation batteries, localized analysis may fail to provide a representative understanding of the bulk material properties. This is a significant limitation when evaluating degradation mechanisms, dendrite formation, or particle-level interactions across an entire solid electrode. For cryo-TEM, radiation damage from high-energy electron beams poses a significant obstacle. Prolonged exposure during imaging can degrade sensitive materials such as Li metal, polymer electrolytes, or sulfide-based solid electrolytes, all of which play critical roles in advanced batteries. Moreover, the complex of cryo-TEM sample preparation presents another challenge. Maintaining cryogenic temperatures throughout the sample preparation process is essential to preventing material degradation and unwanted reactions with atmospheric moisture or oxygen. This intricate procedure requires specialized equipment and expertise, reducing throughput and limiting its adoption for routine battery research.

Recent advancements in both FIB-SEM and cryo-TEM have addressed these challenges. In FIB-SEM, the adoption of cryogenic conditions has proven to be effective in minimizing beam-induced damage. Cryo-FIB-SEM allows the preparation of samples in their native state, preserving sensitive materials such as Li deposits. Furthermore, plasma-focused ion beam systems, which employ ions such as xenon or argon instead of Ga, have enhanced milling efficiency, enabling the analysis of larger sample volumes and improving the characterization of thick electrodes and bulk materials. Similarly, cryo-TEM has benefited from significant innovations, particularly through the integration of cryo-FIB techniques for precise sample preparation. These methods facilitate the extraction of lamellae from specific regions of interest, while maintaining the native structure and interfaces of the material. Advances in detector technology and optimized imaging protocols have also mitigated radiation damage, allowing for longer imaging sessions and higher-quality data acquisition. Together, these developments are expanding the capabilities of FIB-SEM and cryo-TEM, enabling a more accurate and comprehensive characterization of battery materials and interfaces.

RECENT ADVANCEMENTS AND PROGRESS OF IMAGING CHARACTERIZATION IN ASSBS

Recent Progress in Neutron Imaging. NI is an advanced technique that utilizes neutrons to detect the internal structures of samples on a macroscopic scale. This rapidly evolving method has emerged as a powerful and nondestructive tool, particularly in the field of energy storage.[34,47] Unlike X-rays, which are primarily absorbed by heavier elements, neutrons exhibit greater sensitivity to light-Z elements such as H and Li. This characteristic renders NI exceptionally valuable for investigating the dynamics of Li metal SSBs, particularly in monitoring the distribution of the Li gradient throughout the cell volume.

NI can visualize the Li diffusion and electrolyte consumption within the solid-state electrodes and SSEs,[48−50] enhancing our understanding of Li behavior during charging and discharging cycles. Additionally, this technique enables the tracking of the spatial distribution and deformation of Li metal anodes, factors that are intricately linked to the cycling performance of ASSBs.[51] By providing insights into these critical processes, the NI contributes significantly to the advancement of battery technology and the optimization of energy storage systems.

Li-Ion Gradient Distribution in ASSBs. Although both LIBs and ASSBs are generally regarded as "black box" systems, ubiquitous interfaces within ASSBs complicate direct detection more than in LIBs, thereby hindering the observation and understanding of their workings mechanisms and degradation pathways.[52] Specifically, the phenomena occurring in ASSBs—such as ion transport, phase transitions, and electrochemical chemical reactions—occur within solid materials and at their interfaces and are therefore difficult to observe without advanced techniques. Given that the reactions occurring in

https://doi.org/10.1021/acsenergylett.4c02476
ACS Energy Lett. 2025, 10, 496−525

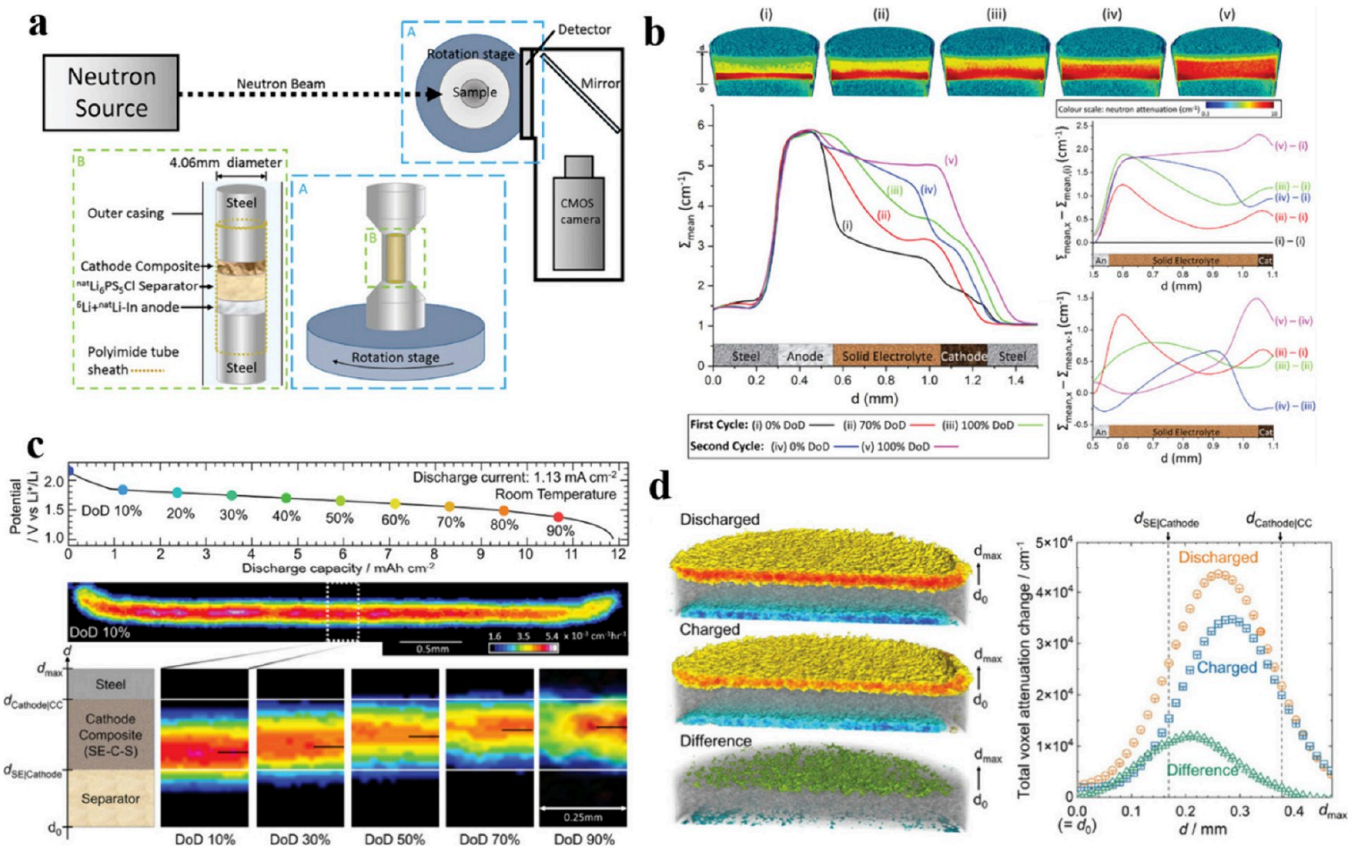

Figure 2. (a and b) The schematic demonstration of the cell and the setup for NI, 3D tomographic image of ^{6}Li propagation and the mean neutron attenuation (Σ_{mean}) changes across the cell at various discharge states. Reproduced with permission.[53] Available under CC BY 4.0. Copyright 2023, Wiley-VCH GmbH. (c and d) The dynamics of Li gradient distribution exhibited by operando NI and 3D rendering images of the discharged and recharged states. Reproduced with permission.[48] Available under a CC BY 4.0. Copyright 2023, Wiley-VCH GmbH.

ASSBs encompass a complex interplay of chemistry, electrochemistry, and mechanics, the ability to visualize these processes is crucial for a comprehensive investigation. Consequently, developing nondestructive and noninvasive tools for operando visualization is essential for comprehending the complicated electro-chemo-mechanical reaction mechanisms inherent to ASSBs.

Our colleagues, Bradbury et al., employed advanced NI techniques to monitor Li-ion transport across multiple layers within a closed all-solid-state Li−S battery (In/Li | Li_6PS_5Cl | S/C/Li_6PS_5Cl) system (ASLSBs).[53] They designed a column cell that could be positioned on a rotational stage (Figure 2a), which allowed for enhanced experimental flexibility and enabled spatial analysis of the sample from multiple angles. As the neutron beam traverses the sample, elements can be distinguished based on their differing interactions with neutrons. This interaction leads to varying contrasts between elements with high neutron absorption and those with low absorption. The two primary isotopes of Li, ^{6}Li and ^{7}Li, can be used to enhance neutron contrast due to their markedly different neutron absorption characteristics: ^{6}Li exhibits approximately 7.6% absorption, while ^{7}Li accounts for about 92.4%. This distinction enabled the clear demonstration of dynamic attenuation changes across the cell compared to its pristine state.[53] The authors tracked ^{6}Li diffusion through the SSE, employing 3D reconstructions to illustrate Li-ion transport and variations in the isotope ratio (Figure 2b, top). This powerful visualization technique effectively mapped the concentration gradients and Li transport pathways within the system. After charge/discharge cycling, certain regions of the SSE separator approached an equilibrium distribution of ^{6}Li, but significant differences remained at the interface. Neutron attenuation as a function of depth (d) was compared for different depths of discharge (DoD) over two cycles, with quantitative results further illustrating the inhomogeneity of variations in the SSE separator (Figure 2b, bottom).

In addition, Bradbury et al. used the NI technique to monitor the spatial distribution of Li and identify the rate-limiting steps in the ASLSBs. This analysis is crucial for pinpointing critical bottlenecks and facilitating the design of highly loaded composite cathodes. Figure 2c presents *operando* 2D neutron radiography images of ASLSB at various DoD.[48] The rate of change in neutron attenuation can be calculated and is depicted using different color brightness levels, effectively demonstrating the local dynamic transport of Li through the composite cathodes. Notably, the "reaction front", which corresponds to the maximum attenuation rate, gradually advances from the SSE side toward the current collector upon discharging. While 2D radiography provides dynamic information on Li-ion transport as a function of d, 3D neutron tomography is reconstructed by collecting a set of 2D images as the cell rotates. To directly observe changes in the Li distribution throughout the volume, the authors subtracted the pristine state from both the fully discharged (top) and charged (middle) states (Figure 2d). The loss of Li on the anode side due to discharge and charge cycles leads to a negative attenuation change, while the separator region, shown in gray, exhibits zero net change in Li amount, indicating a stable Li concentration within the SSE. In the fully

https://doi.org/10.1021/acsenergylett.4c02476
ACS Energy Lett. 2025, 10, 496−525

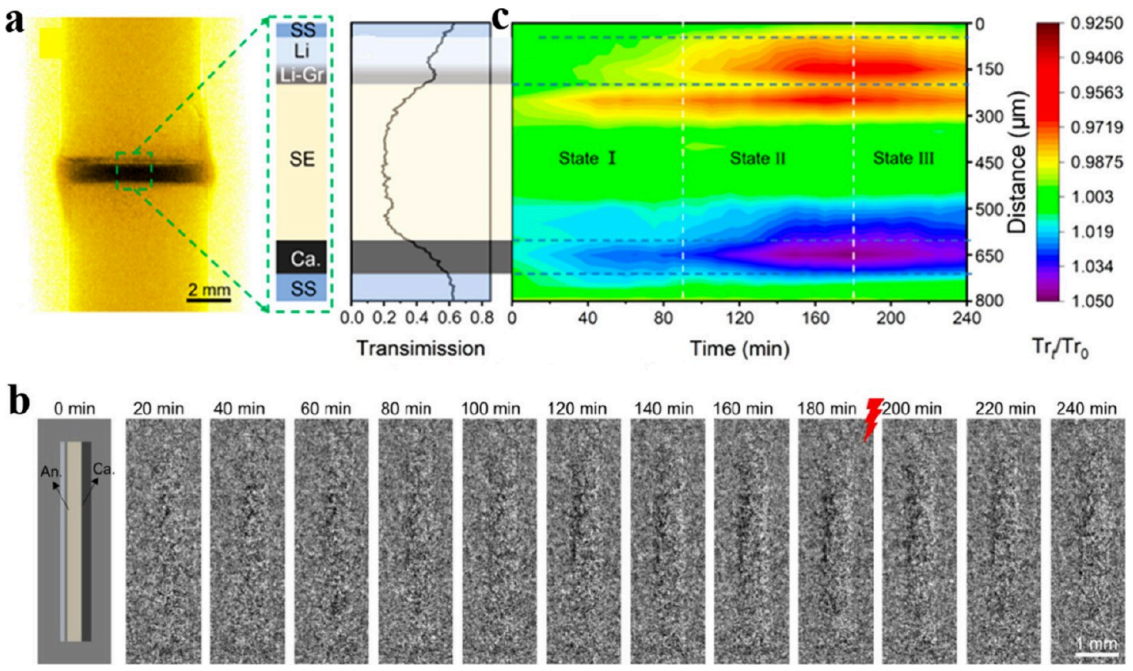

Figure 3. (a) 2D neutron radiography images of ASLMB to discern each component based on neutron attenuation differentiation. (b) Quantified neutron transmission along the labeled region of the ASLMB cross section. (c) Dynamic evolution of Li during charging. Reproduced with permission.[50] Available under CC-BY 4.0. Copyright 2024, American Chemical Society.

discharged state, an increase in Li concentration within the composite sulfur cathode suggests the formation of Li_2S. In the charged state, the Li concentration in the cathode region remains elevated compared to the initial state, implying that Li_2S has not been completely reduced back to S—a phenomenon that is closely correlated with the capacity loss. As shown in the right panel of Figure 2d, the composite cathode exhibits a heterogeneous Li distribution. It is noteworthy that on the cathode side, from d_0 to d_{max}, the peak of the attenuation change (Figure 2d) in the charged state is closer to the current collector than that in the discharged state. This difference, represented by the green plot, suggests that Li^+ ions migrate back to the Li anode during charging, with Li losses primarily originating from the composite cathode near the SSE separator side rather than from the current collector side. In the composite cathode, the electronic conductivity near the collector side is superior near the SSE separator side, while the ionic conductivity is greater near the SSE separator side. When the effective electronic conductivity exceeds the ionic conductivity, a "reaction front" phenomenon occurs, migrating from the separator side to the collector side, which is consistent with experimental observations. This further impedes delithiation from the collector side, contributing to a heterogeneous distribution of Li and exacerbating Li loss.

To enhance the compatibility of the Li anode with sulfide-type SSE, Cao et al. introduced a mixed ionic-electronic conductor (MIEC) and employed operando NI to study Li dynamics.[50] Figure 3a shows the 2D neutron radiograph image of the ASLMB, revealing a layered structure. The neutron transmission distribution along the axial direction can help distinguish the interfaces between adjacent layers (Figure 3b). The transmission change ratio, Tr_t/Tr_0, was employed to assess the evolution of the Li concentration. This ASLMB failed after 180 min of charging, with the voltage quickly dropping to a low value, indicating a "hard short". Figure 3b presents time-stamped images after processing the transmission data in Figure 3a. The fluctuations in the transmission change ratio, along with the corresponding colors, clearly illustrate the changes in Li concentration: when $Tr_t/Tr_0 > 1$, indicating reduced Li concentration, the region is shown in bright colors; when $Tr_t/Tr_0 < 1$, indicating increased Li concentration, the region appears darker; when $Tr_t/Tr_0 = 1$, a gray color signifies no change in Li concentration. Due to the low contrast in these images, transmission intensity mapping was used to provide more detail (Figure 3c). The colors represent changes in Li transmission: blue indicates Li depletion ($Tr_t/Tr_0 > 1$), red means Li enrichment ($Tr_t/Tr_0 < 1$), and green shows no change in Li concentration ($Tr_t/Tr_0 = 1$). This investigation reveals that while the cathode experiences lithium depletion, the anode exhibits lithium accumulation. Specifically, the charging process unfolds in three distinct stages (Figure 3c). At Stage I (0−90 min), the Li concentration increases primarily at the Li-graphite|SE interface. As Li-graphite partially penetrates the SSE layer, surface voids accommodate plated lithium (Li^0), leading to Li enrichment on the SSE side. At Stage II (90−180 min), Li continues to concentrate at the Li-graphite|SE interface, within the Li-graphite interface, and in the Li^0 regions, indicating that Li^+ ions can migrate across the Li-graphite layer. At Stage III (after 180 min), the ASLMB experiences short circuits. Although charging continues, the cell exhibits an inverse Li concentration trend: the anode loses Li, and the cathode gains it.

In addition to *operando* 2D neutron radiography imaging, *ex situ* 3D CT scans of the ASLMB were performed before and after the electrochemical test to capture the spatial evolution of Li.[51] The 3D structure of the ASLMB before cycling is illustrated, showing a clear depiction of the ASLMB. Following the electrochemical reaction, the changes in Li concentration were analyzed by using subtraction treatment, revealing Li enrichment on the anode side. To examine this in more detail, three slices from 3D tomography data were used to extract the cross-sectional morphology of the Li. It was observed that Li expanded at the top and bottom while shrinking in the middle. The

https://doi.org/10.1021/acsenergylett.4c02476
ACS Energy Lett. 2025, 10, 496−525

expansion in the top region contributed to the deformation of the Li. Cross-section of ASLMB's tomography image shows the positions of different components. In summary, NI enables nondestructive monitoring of Li concentration changes through 2D radiography and allows the tracking of Li spatial changes via 3D CT. Additionally, Li deformation has been observed using this technique, highlighting the crucial role of external pressure in reducing dendrite growth rates.

However, it is important to acknowledge the limitations of even the most advanced technology. For instance, detecting Li dendrites within SSEs remains a significant challenge due to the limited spatial resolution of NI techniques and the microscale size of pores or cracks within these materials. Fortunately, XRT offers a promising solution to these limitations by providing higher resolution and detailed morphological information, making it an invaluable tool for investigating the buried interfaces within ASSBs. Notably, XRT can achieve a spatial resolution on the order of tens of nanometers, effectively bridging the gap left by NI (>10 μm). The integration of these complementary methods is expected to offer crucial insights into the morphological and structural evolution of the interfaces within ASSBs at scales ranging from macroscopic to microscopic.

Recent Progress in Synchrotron X-ray Tomography. X-ray tomography (XRT) emerges as an advanced imaging technique capable of visualizing the internal 3D structure of samples.[54] By capturing detailed cross-sectional images of an object from various angles and reconstructing the 3D images through computer algorithms, XRT can nondestructively image the buried interfaces,[55,56] which is expected to be a powerful tool for studying and understanding the working and failure mechanisms of ASSBs.[41,57] In this section, we highlight recent studies employing XRT to probe the structural evolution and chemical stability of the SSEs, Li anode, and cathode as well as their interfaces within ASSBs.

SSE Cracking and Failure Mechanism. The nonflammable SSEs are thought to mechanically prevent the propagation of Li dendrites, particularly for inorganic SSEs with relatively high shear modulus (G). Employing the linear elasticity theory, Monroe and Newman reported that SSE has a G-value twice that of metallic Li ($G_{Li} \approx 4$ GPa), which should be sufficient to inhibit dendrite growth.[58] According to the Monroe–Newman theory, SSEs with G_{SSE} greater than 8 GPa can prevent dendrite formation. Most oxide-based SSEs have a G-value between 40 and 60 GPa, which is 10 times higher than that of Li metal; therefore, they should theoretically be hard enough to inhibit dendrite penetration.

However, commonly used SSEs, such as oxide-based $Li_7La_3Zr_2O_{12}$ (LLZO) and sulfide-based $Li_{10}GeP_2S_{12}$ (LGPS), fail to effectively suppress Li dendrite growth.[69] This limitation is particularly evident in sulfide-based SSEs due to their relatively low shear modulus ($G_{LPS} = 7.1 \pm 0.3$ GPa). It should be noted that the criterion proposed by Monroe and Newman, which is based on shear modulus, is mainly applicable to polymer electrolytes and SSEs that lack inhomogeneities or defects.[70,71] This criterion, therefore, has limited applicability in understanding dendrite growth mechanisms. Li dendrites tend to form within SSEs, particularly at GB, voids, and other defects. Thus, understanding the mechanical properties of SSEs and their role in Li metal nucleation and penetration becomes critical.

We summarize the key mechanical properties of SSEs in Table 2, highlighting the significant discrepancies between different SSE types. Specifically, oxide-based SSEs demonstrate much greater stiffness compared to sulfide-based SSEs. For instance, Young's modulus (E), which reflects a material's resistance to elastic deformation, can be converted into G using the equation $G = E/2(1 + \nu)$, where ν is Poisson's ratio.[72] The differences in mechanical properties among SSEs underscore their varying capacities to resist fracture (Table 2), as illustrated by fracture toughness (K_{IC}). When the electrochemically induced stress exceeds the K_{IC} threshold of an SSE, cracks may form, impeding local ionic migration and increasing cell polarization.[72]

Table 2. Summary of Mechanical Properties of Different SSEs

Solid-state electrolytes	Young's Modulus (E, GPa)	Hardness (H, GPa)	Fracture toughness (K_{IC}, MPa·m$^{1/2}$)	ref.
$Li_{1.5}Al_{0.5}Ge_{1.5}(PO_4)_3$ (LAGP)	75–101	3.7–5.3	–	59
$Li_{1.3}Al_{0.3}Ti_{1.7}(PO_4)_3$ (LATP)	81–115	7.1	1.1	60
$Li_{6.6}La_3Zr_{1.6}Ta_{0.4}O_{12}$ (LLZTO)	151–157	5.1	1.28	61, 62
$Li_{6.91}Al_{0.13}La_3Zr_2O_3$ (LALZO)	135–140	4.3–9.1	1–1.3	63
$Li_{0.33}La_{0.57}TiO_3$ (LLTO)	186–200	–	0.89–1.34	64
$Li_7La_3Zr_2O_{12}$ (LLZO)	140	7.3–8.9	0.87–1.07	63
$LiTi_2(PO_4)_3$	143.7	–	–	65
Li_6PS_5X (X = Cl, Br, I)	22–30	–	–	65
$Li_{10}GeP_2S_{12}$	37.2	–	–	66
Li_3PO_4	77	3.9	–	67
$Li_2S–P_2S_5$	18	–	0.23 ± 0.04	68
$Li_xPO_yN_z$	77	4	–	67

It is worth noting that the heterogeneity of electrolytes—such as porosity, defects, SSE density, and grain size—can lead to variations in the mechanical stress distribution and fracture behavior within SSEs. Fortunately, XRT can provide a nondestructive characterization by leveraging the different attenuation coefficients of X-rays for various materials, as described by the Lambert–Beer law.[73,74] Due to the differing X-ray attenuation properties of various materials and components, XRT can effectively reveal buried structures such as voids, cracks, Li dendrites, and newly formed interphases that contribute to battery degradation.

Dixit et al.[73] systematically investigated the effects of these factors on interphase chemistry and fracture inhomogeneities. In their study, kinetically metastable interphases were engineered by iodine doping (LPS:0.5LiI), and microstructural control was achieved through milling (LiI-AT) and annealing (LiI-AN) techniques. *In situ* XRT was used to visualize the facture initiation and propagation in various samples (A-LPS, LPS:0.5LiI, LiI-AT and LiI-AN). As shown in Figure 4a, two primary failure modes were identified across all samples, i.e., (I) edge-chipping failure at the Li/SSE interface and (II) vertical crack propagation from the edge-chip along the SSE thickness. While the crack formation mechanisms were consistent across the four LPS materials, the extent of crack propagation varied significantly, suggesting that lateral fractures in LPS tend to expand more aggressively in regions of higher porosity, which is influenced by microstructural heterogeneity. Increased porosity enhances local curvature, which, in turn, increases local current density and electric field, thereby accelerating crack propagation. Hatzell et al.[74] explored pore connectivity in ceramic electrolytes, such as LLZO, using XRT. Their finding revealed that samples sintered at 1150 °C exhibited reduced porosity and a

https://doi.org/10.1021/acsenergylett.4c02476
ACS Energy Lett. 2025, 10, 496–525

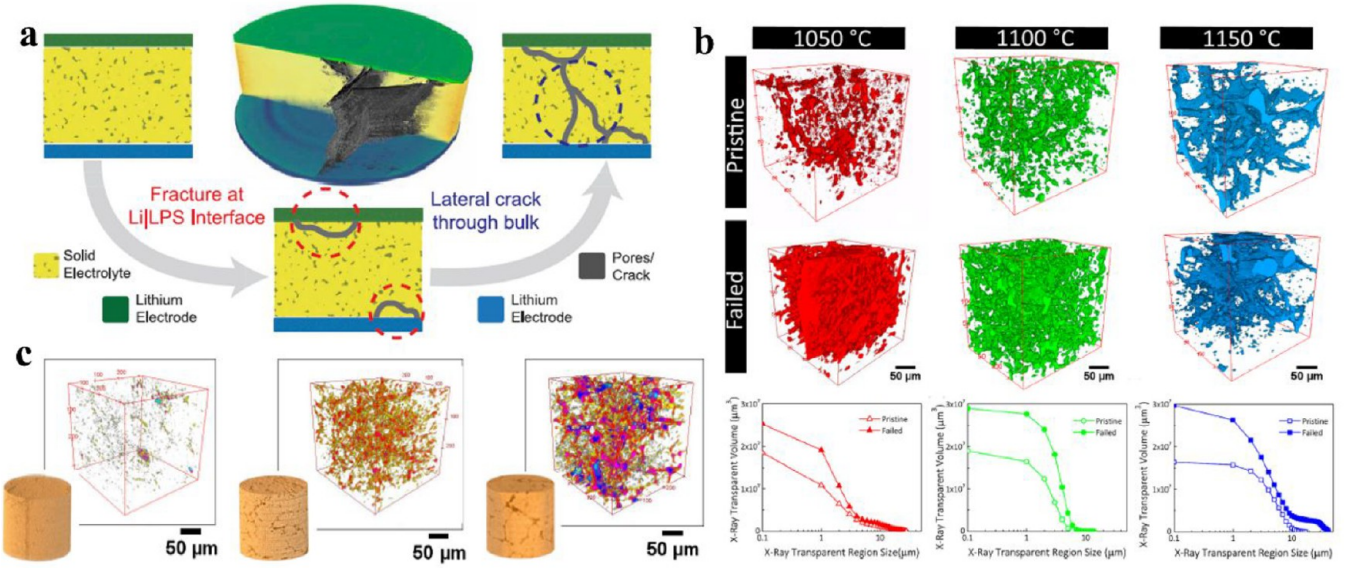

Figure 4. (a) The degradation initiation and growth mechanism in LPS-based SSEs. Reproduced with permission.[73] Copyright 2020, Elsevier. (b) Morphological changes in LLZO, including void phase reconstructions and changes in pore size distribution. Reproduced with permission.[74] Copyright 2018, American Chemical Society. (c) Pore-size color maps, representing the size of pores in the microstructure of LLZO sintered at different temperatures. Reproduced with permission.[75] Copyright 2018, American Chemical Society.

broader distribution of pore sizes compared to those sintered at 1050 °C (Figure 4b). Additionally, structural changes in LLZO SSEs caused by electrochemical cycling were monitored, confirming improvements in the pore connectivity. These void regions contribute to the formation of highly tortuous channels within the SSEs, leading to increased local concentration and polarization gradients, which ultimately promote the formation and growth of Li dendrites.

Additionally, the tortuosity of SSEs has a profound effect on Li-ion transport behavior. To evaluate tortuosity comprehensively, Hatzell et al.[75] employed a combination of computational fluid dynamic simulations and XRT data analysis to study the tortuosity of LLZO sintered at temperatures ranging from 1050 to 1150 °C (Figure 4c). Specifically, XRT was utilized to extract segmented binary phase structures, which were then imported into COMSOL for a detailed analysis. Their results demonstrated that LLZO synthesized at 1150 °C exhibited significant anisotropy and tortuosity, leading to an inhomogeneous distribution of ion flux and a pronounced local polarization gradient. However, achieving fully dense electrolytes with zero porosity remains extremely challenging, which requires high-energy and high-temperature sintering processes or novel fabrication techniques. Therefore, tuning the microstructure of SSEs, particularly by controlling the pore size and distribution, is anticipated to be crucial for realizing high-performance ASSBs.

Previous studies have primarily focused on the structural and morphological changes within bulk LLZO electrolytes and pore regions, while the propagation of Li dendrites and voids in SSBs has been less explored. Distinguishing Li dendrites from neighboring voids or cracks is particularly challenging. First, the image contrast between Li and voids in dense SSEs is minimal due to their similar low X-ray attenuation. Second, imaging dense SSEs, especially those with garnet electrolytes containing high *Z*-elements (such as La, Zr, and doped Ta or Ge), requires high-energy X-rays, while visualizing Li metal typically necessitates low-energy X-rays, complicating the differentiation among Li dendrites, pores, and cracks.

Notably, Hao et al.[76] used high-resolution X-ray nano computed tomography to observe the 3D morphology of Li protrusions ("dendrites") within garnet-based $Li_{6.6}La_3Zr_{1.6}Ta_{0.4}O_{12}$ (LLZTO). Improved image contrast allowed for clear segmentation of Li, LLZTO, and cracks (Figure 5a). They found that Li protrusions primarily propagate intergranularly along GB in LLZTO, forming wave-like patterns. Interestingly, Li protrusions preferentially grew in regions with a lower curvature within the cracks. Quantitative analysis revealed that 82.0% of cracks were filled with Li, compared to 57.3% of the pores formed during fabrication, indicating that Li is more likely to fill cracks than pre-existing pores. This suggests that simply reducing the porosity of the LLZTO may not completely prevent Li dendrite propagation.

To further investigate the relationship between crack development and Li dendrite growth during battery operation, *in situ* phase-contrast XRT has been used to visualize the progression of Li dendrites in $Li/Li_6PS_5Cl/Li$ cells.[82,83] During Li plating, conical pothole-like cracks, termed spallation, emerged near the Li_6PS_5Cl/plated electrode interface and propagated through the ceramic electrolyte ahead of the Li dendrites. The spallation continued to grow as more Li was plated into the cracks, ultimately causing a short circuit when the cracks were fully occupied by Li. Similarly, Hao et al. used in situ XRT[77] to observe thin-sheet cracks originating from the Li/Li_3PS_4 interface, which penetrated the SSE after the 2nd plating and led to a short-circuit after the 14th plating (Figure 5b). They noted that Li growth lagged behind crack propagation, resulting in hollow cracks on the cathode side. A groundbreaking study by Ning et al.[84] has shown that Li dendrite initiation and propagation are two separate processes, each critically contributing to battery failure. *Operando* XRT imaging revealed that dendrite initiation occurs when Li deposits in the subsurface pores and causes microcracks. By identifying the factors that influence both processes, such as the local fracture strength at GB, SSE porosity, current density, stack pressure, and the macroscopic fracture toughness of SSEs, researchers can better target methods to mitigate dendrite growth.

https://doi.org/10.1021/acsenergylett.4c02476
ACS Energy Lett. 2025, 10, 496−525

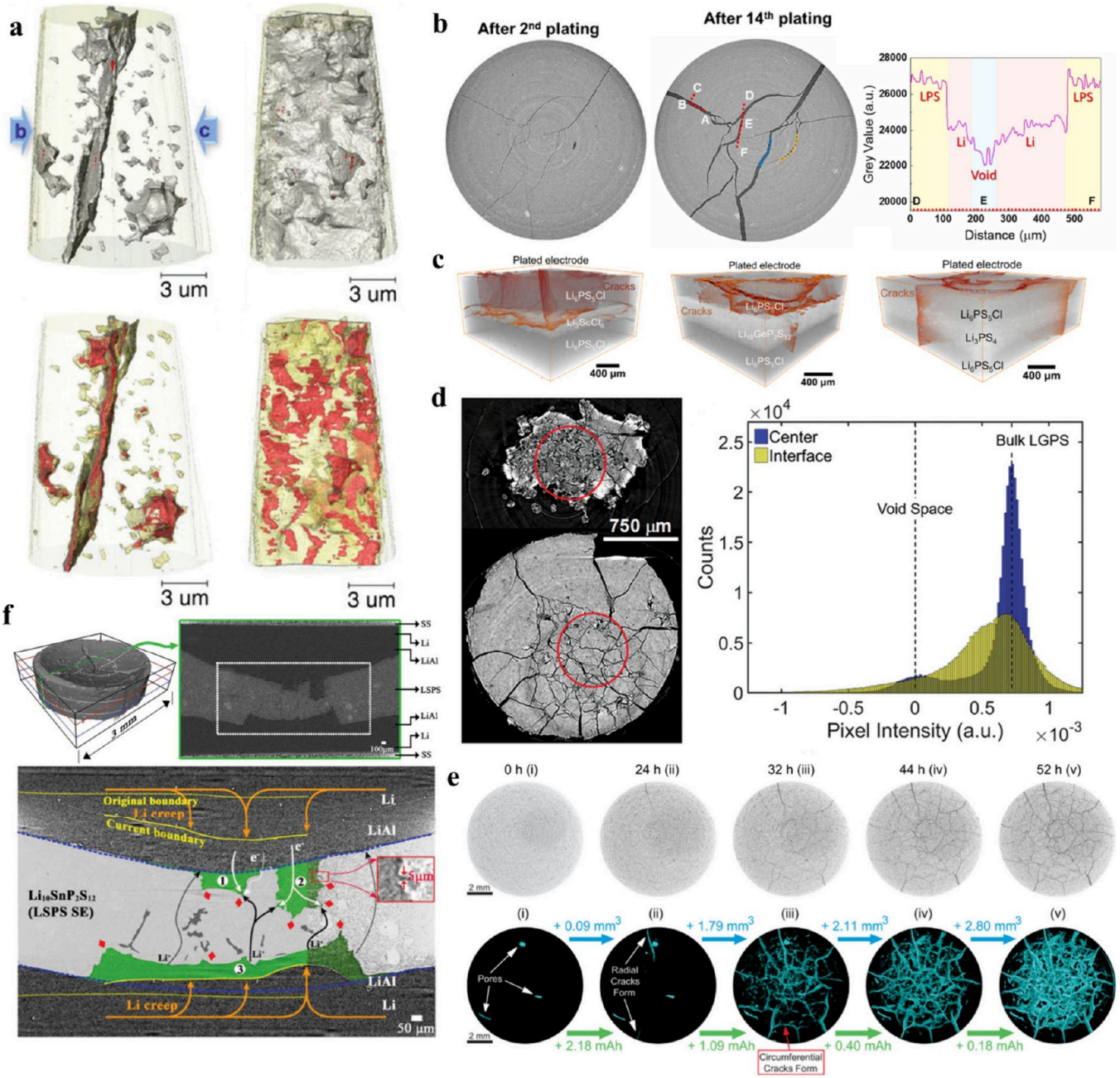

Figure 5. (a) 3D rendering of degraded LLZTO phase that contains internal Li protrusions (opaque gray) and voids (red), viewed from various directions. Reproduced with permission.[76] Copyright 2020, Wiley-VCH GmbH. (b) Virtual slices after plating and the grayscale profile along several lines. Reproduced with permission.[77] Copyright 2021, Elsevier. (c) 3D rendered demonstrations of crack deflection along Li_6PS_5Cl/Li_3ScCl_6, Li_6PS_5Cl/$Li_{10}GeP_2S_{12}$, and Li_6PS_5Cl/Li_3PS_4 interface after plating, respectively. Reproduced with permission.[78] Available under a CC BY 4.0. Copyright 2024, Elsevier. (d) Reconstructed tomographic images acquired from the LGPS/Li^0 interface and histograms of corresponding pixel intensities. Reproduced with permission.[79] Copyright 2020, Wiley-VCH GmbH. (e) 2D slices of LAGP after different cycling states were extracted from 3D tomograms. Reproduced with permission.[80] Copyright 2019, American Chemical Society. (f) 3D volume rendering of the LSPS and a selected cross-sectional slice showing the (electro)chemically generated interphase, Li creep direction, as well as potential transportation pathways of Li^+/electrons. Reproduced with permission.[81] Copyright 2022, Wiley-VCH GmbH.

To prevent Li dendrite propagation, Hu et al.[78] evaluated multilayer SSE structures using different solid electrolytes, such as Li_3ScCl_6 and $Li_{10}GeP_2S_{12}$, as inner layers sandwiched between outer layers of argyrodite Li_6PS_5Cl due to their high ionic conductivities. Li_3PS_4 was also studied as an inner layer due to its elastic modulus similar to that of Li_6PS_5Cl. Both Li_3ScCl_6 and $Li_{10}GeP_2S_{12}$ effectively deflected Li dendrite cracks at the interface with Li_6PS_5Cl, due to significant differences in Young's modulus, creating a weak mechanical interface (Figure 5c). It should be noted that the correlation between Li protrusion growth and crack propagation is complicated, involving concurrent electrochemical and mechanical processes. *Operando* XRT was used to investigate the mechanical responses of $Li_{10}GeP_2S_{12}$ (LGPS) during cycling.[79] The electrochemical reduction of LGPS during Li plating led to the formation of low-density domains at the Li/SSE interface (Figure 5d), inducing compressive stress on LGPS and ultimately leading to cracking. The critical shear stress for fracture was estimated at

https://doi.org/10.1021/acsenergylett.4c02476
ACS Energy Lett. 2025, 10, 496−525

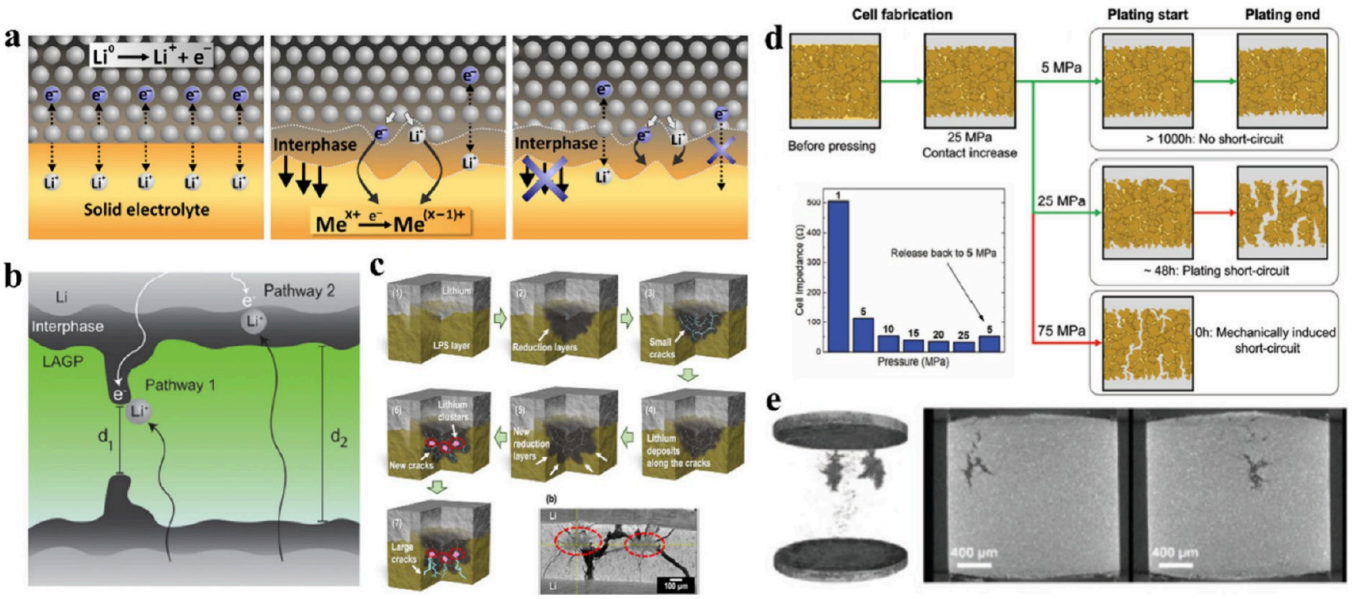

Figure 6. (a) Three types of interfaces between Li metal and the different solid Li^+ ions conductors. Reproduced with permission.[89] Copyright 2015, Elsevier. (b) Schematic illustration of nonuniform growth of the mixed-conducting interphase. Reproduced with permission.[90] Copyright 2019, American Chemical Society. (c) Crack formation mechanism that starts at the Li/LPS interface and a tomographic view of the Li/LPS/Li cell after short-circuiting. Reproduced with permission.[91] Copyright 2021, American Chemical Society. (d) Schematic representation of the impact of stack pressure on the $Li/Li_6PS_5Cl/Li$ SSBs short-circuit behavior; (e) tomographic images indicate that a few low-density dendrites formed in the electrolyte after short-circuiting at 25 MPa stacking pressure. Reproduced with permission.[92] Copyright 2019, Wiley-VCH GmbH.

approximately 0.8 ± 0.2 GPa, much lower than the shear modulus required to prevent dendrite formation. This suggests that electrochemical instability at the Li/SSE interface significantly compromises mechanical stability, promoting dendrite formation.[62,85]

In NASICON-type SSEs, Li penetration and interphase growth induce significant volume expansion, creating internal stress that damages the SSE and increases resistance. *In situ* XRT visualizations of $Li_{1+x}Al_xGe_{2-x}(PO_4)_3$ (LAGP) SSEs revealed a dramatic volume expansion of approximately 130% during interphase growth. This expansion was shown to create web-like cracks, which primarily contribute to increased impedance rather than being directly caused by the resistance of the interphase itself (Figure 5e).[80] Simulations of mechanical stress in the LAGP further elucidated the role of internal stresses in crack formation. Radial and circumferential stress components were identified as key drivers, with stress concentrations at the reacted interphase edge acting as the initiation sites for radial crack propagation throughout the SSEs. Similarly, in LiSnPS SSEs, the mechanical stresses were observed and quantified following a single discharge.[81] High-resolution 3D renderings and 2D resliced images from XRT revealed significant mechanical deformation in the LiSnPS SSE. These included irregular cracks within the SSE and wedge-shaped cracks along the SSE interface. The formation of these cracks was attributed to accumulated strain energy and electro-chemo-mechanical coupling. Calculations further revealed that mechanical stresses induced by an overpotential of $\Delta\Phi = 100$ mV were sufficient to initiate and propagate cracks within the SSE, ultimately compromising its structural integrity.

Li/SSE Interface. The utilization of Li metal anodes represents a promising avenue for enhancing the energy density of the ASSBs. However, the integration of Li metal with SSEs introduces a range of structural degradations at their interfaces, which are among the primary causes of cell short-circuit. The nondestructive capabilities of XRT provide a powerful means of probing the Li/SSE interfaces, enabling 3D visualization of buried interfaces without requiring cell disassembly.[57,86] Recent advancements in XRT have facilitated the identification of several types of morphological degradations at the Li/SSE interfaces including Li dendrite nucleation/propagation, interphase growth, and void formation. These insights are critical for understanding and addressing interfacial challenges in improving the stability and performance of ASSBs.

Formation of Li Dendrites at the Li/SSE Interface. Harry et al.[82] utilized XRT to investigate the morphology of dendrites in Li/polymer/Li batteries cycled at 90 °C. Their findings revealed that dendritic structures were embedded within the Li electrode, indicating that the formation of these subsurface structures drives early dendrite development. This highlights the importance of eliminating internal cavities in Li electrodes to prevent dendrite growth. Similarly, Sun et al. used *in situ* XRT to observe morphological and compositional changes occurring at the indium−lithium/thio-LISION (InLi/LISION) electrolyte interface,[87] revealing the growth of InLi protrusions. These studies emphasize the need for time-resolved probes to understand the redox processes and ion transport dynamics in ASSBs.[88]

Instabilities of Li/SSE Interface. The interface between Li and the SSEs is a critical source of instability in ASSBs. Most SSEs, including NASICON-type and sulfide-based SSEs, are chemically unstable when in contact with Li metal, leading to the formation of an interphase at the Li/SSE interface. The morphology, structure, and ion transport properties of this interphase play a pivotal role in determining the electrochemical performance of ASSBs.[57,93,94] Specifically, Li/SSE interfaces can be categorized into three types based on their thermodynamic and kinetic stability: (1) thermodynamically stable interfaces

https://doi.org/10.1021/acsenergylett.4c02476
ACS Energy Lett. 2025, 10, 496−525

without interphase formation, (2) unstable interfaces with a mixed ionic-electronic conductor (MCI) interphase, and (3) unstable interfaces with an ion-conducting, electronically insulating interphase (Figure 6a).[93,94] Each type presents distinct challenges and implications for battery performance.

Lewis and co-workers[90] demonstrated the formation of an MCI at the Li/$Li_{1.4}Al_{0.4}Ge_{1.6}(PO_4)_3$ (Li/LAGP) interface, where Li-ions and electrons reduce LAGP at the interphase boundaries, causing interphase layer growth. Preferential Li deposition occurs in regions with shorter transport paths, as illustrated by pathway 1 in Figure 6b, resulting in uneven interphase development.[95] Over time, as the entire SSE is reduced to MCI, a short circuit occurs, making the failure of the cell.[89] Similar behavior has been observed in sulfide-based SSEs, such as Li_3PS_4, where contact with Li leads to the decomposition of Li_3PS_4 into Li_2S and Li_3P, forming an ionically conductive but electronically insulating reduction layer. While the reduction layer initially prevents continuous interphase growth, repeated decomposition and the associated volumetric expansion create cracks in the SSE. These cracks allow Li penetration into the electrolyte, ultimately resulting in short circuits. This behavior highlights the need for improved chemical and mechanical stability at the Li/SSE interface to prevent degradation and ensure long-term battery performance.

Formation of Voids at the Interface. In addition to short circuits resulting from interphase formation, void formation at the Li/SSE interface during Li stripping poses a significant challenge to the practical implementation of ASSBs.[96,97] Voids develop when Li is stripped from the interface more quickly than it can be replenished, leading to nonuniform deposition during subsequent plating.[98] Over time, these voids exacerbate contact loss, increase localized current densities, and ultimately promote dendrite formation and battery failure. The interplay between void formation and interphase evolution further accelerates the degradation process. *Operando* XRT investigations by Lewis et al.[57] demonstrated that voids at the Li/SSE interface led to increased surface roughness, reduced contact area, and higher interface resistance as illustrated by the following equation:[99]

$$R = \frac{\rho l}{A} \tag{7}$$

Here, R is the resistance, A is the contact area, ρ is the resistivity, and l is the length. This progression creates a self-reinforcing cycle of deterioration, with void-induced roughness worsening the uniformity of Li deposition and interphase development. Addressing void formation has been the focus of various studies, with one proposed solution being the application of stack pressure to improve Li/SSE contact and reduce interfacial resistance.[99−101] For example, Kasemchainan et al.[98] demonstrated that increasing stack pressure improved the critical current density (CCD), below which dendrite formation does not occur. Their findings showed that a stack pressure of 3 MPa allowed for a maximum current density of 0.2 mA cm^{-2} without void formation. However, an excessive stack pressure can have detrimental effects. Masias et al.,[102] observed that applying pressure beyond the yield strength of Li (∼0.8 MPa) caused Li metal to undergo creep, leading to mechanical instability and premature cell failure. LePage and co-workers[103] further investigated Li creep behavior, identifying two primary creep mechanisms: diffusional creep, which occurs at very low stresses due to atomic diffusion along grain boundaries, and power-law creep, which dominates at higher stress levels due to its strong stress dependence.[72]

To evaluate the influence of stack pressure on the electrochemical performance of ASSBs, researchers studied three symmetric Li/Li_6PS_5Cl/Li cells under varying stack pressure of 5 MPa (low), 25 MPa (intermediate) and 75 MPa (high) as displayed in Figure 6d.[92] Under a low stack pressure of 5 MPa, the cells achieved stable plating and stripping cycles for over 1000 h without short-circuiting. At 25 MPa, the cell was operated for 48 h before failure. In contrast, high stack pressure (75 MPa) caused mechanical short-circuiting even before cycling began, as the stress—approximately 100 times higher than the yield strength of Li—accelerated the formation of conductive pathways via power-law creep. XRT results further revealed that excessive stack pressure could fracture SSEs, exacerbating mechanical degradation (Figure 6e). However, the stack pressure applied to ASSBs is not constant during cycling due to the volume changes in the solid electrodes, indicating that the internal stack pressure within the cell may differ from the initially applied stack pressure.[40,96,104] Real-time monitoring of stack pressure in ASSBs with LiPSCl and $Li_{10}SnP_2S_{12}$ (LSPS) by Chanhee et al.[101] revealed its dynamic nature and its correlation with interphase formation and morphological evolution. Their study demonstrated that at the Li/LSPS interface, the formation of a thick MCI interphase (type II) during cell operation leads to a significant volume reduction in the cell stack due to partial molar volume mismatches. This results in a decrease in the stack pressure within the confined cell system. Conversely, a thin, electronically insulating interphase (type III) at the Li/LPSCl interface results in minimal volume reduction and better pressure. These findings underscore that changes in stack pressure are closely tied to the chemical stability of the Li/SSE interface.

Stack pressure also plays a crucial role in the cycling performance of garnet-type oxide electrolytes (LLZO), which are highly stable against Li metal.[105] Wang et al.[99] evaluated the influence of stack pressure and current density on the response of potential of symmetric Li/LLZO/Li cells during galvanostatic cycling. They found that at current densities exceeding 0.1 mA cm^{-2}, a substantial potential increase was observed at low stack pressures, whereas the potential remained relatively stable under higher stack pressures. This observation suggests a critical stack pressure, defined as the pressure at which the incoming Li flux supplied by stack pressure balances the Li flux dissolving and migrating through the LLZO. Below the threshold, inadequate stack pressure fails to replenish Li at Li/LLZO interface, allowing voids to form and grow. Above the critical stack pressure, sufficient stack pressure promotes Li creep toward the interface, preventing substantial void formation. The formation of voids at the interface of ASSBs is thus detrimental, which may dramatically reduce the Coulombic efficiency and cycle life of the cell. However, it has been revealed here that voids can only develop and result in significant impact on potential behavior at stack pressures lower than the critical stack pressure. This implies that the applied stack pressure is a critical parameter when engineering ASSBs for long life and high-rate capability. In summary, external stack pressure applied to ASSBs appears to be a double-edged sword. On the one hand, it is necessary to prevent the formation of voids during Li stripping.[106,107] On the other hand, both experimental[92] and theoretical[108] investigations demonstrate that excessive pressure can accelerate premature cell failure by amplifying mechanical stress. Thus, optimizing stack pressure is crucial for balancing improved interfacial stability with minimized mechanical degradation,

https://doi.org/10.1021/acsenergylett.4c02476
ACS Energy Lett. 2025, 10, 496−525

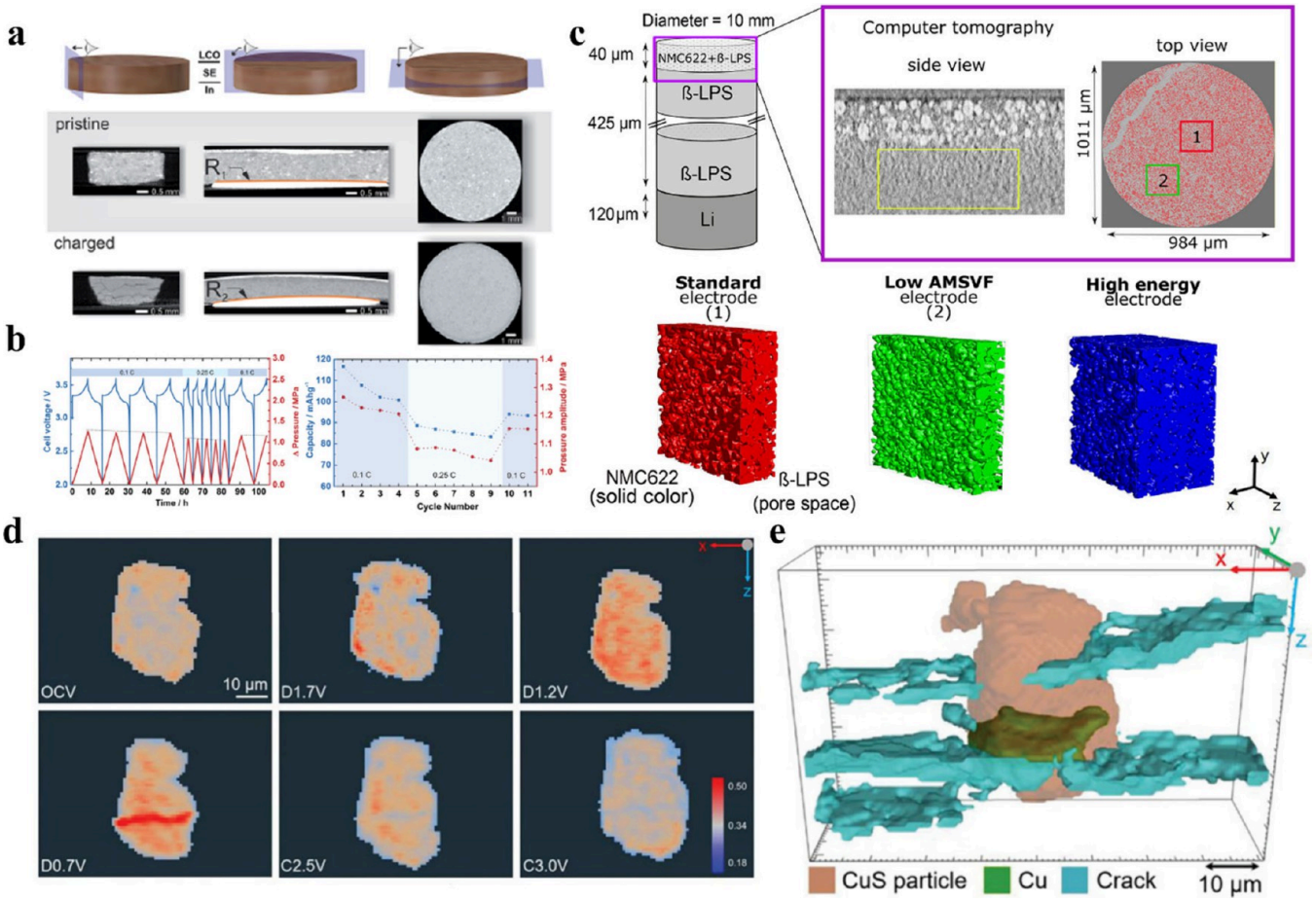

Figure 7. (a) *Ex situ* XRT image slices of the pristine and postcharged In/LGPS/LCO SSBs. Reproduced with permission.[104] Copyright 2017, The Royal Society of Chemistry. (b) Pressure change profiles of an LTO/LGPS/LCO SSB during galvanostatic cycling. Reproduced with permission.[104] Copyright 2017, The Royal Society of Chemistry. (c) Schematic diagrams of cell setups and 3D microstructure reconstructions of the distribution of active material in different regions. Reproduced with permission.[114] Copyright 2020, American Chemical Society. (d and e) The virtual cross sections of the CuS cathode particles show the microstructure in different SOC states during first discharge and charging and 3D volume rendering of lithiated CuS, cracks, and Cu inclusion. Reproduced with permission.[40] Available under a CC BY 4.0. Copyright 2022, Wiley-VCH GmbH.

ultimately enhancing the performance and longevity of the ASSBs.

Cathode/SSE Interface. Compared with the Li/SSEs interface, the degradation mechanisms at the cathode in ASSBs have received less attention. Unlike liquid electrolytes, which offer excellent wettability, the SSEs suffer from poor solid−solid contact due to their rigidity. To overcome this limitation, composite cathodes are fabricated by intermixing ionic and electronic conductors (SSEs and conductive additives) with cathode active materials (CAMs) to establish efficient conductive pathways for both Li^+ ions and electrons. However, challenges such as uneven mixing, mutual diffusion of ions, and mechanical failure can arise during preparation and cycling, negatively affecting electrochemical performance. Understanding the structural and morphological evolution at the interface between SSEs and CAMs is crucial for unveiling the degradation mechanism in ASSBs.

During cycling, the original composition and structure of the ASSB system undergo dynamic changes, leading to issues such as cracking in the active materials, volumetric changes, and other chemical or mechanical transformations. For example, the lithiation and delithiation processes induce phase transitions that result in lattice expansion and contraction, creating internal strain and stress between the CAMs and SSEs.[109] In the confined environment of ASSBs, this mechanical stress is exacerbated by the rigid coupling between CAMs and SSEs, unlike conventional liquid electrolyte batteries where chemical expansion or compression of CAMs can be more easily accommodated and buffered.[93,110] This mechanical strain underscores the advantages of sulfide-based SSEs, which have a lower Young's modulus (18−25 GPa) and greater compressibility compared to the oxide-based SSEs.[111] The lower rigidity of sulfide SSEs offers flexibility and deformability, helping to reduce mechanical stress and maintain close ionic contact during cathode material expansion. In contrast, oxide-based SSEs, such as garnet oxides, have a much higher Young's modulus (up to 150 GPa), making them more rigid and less capable of maintaining continuous Li-ion pathways within the CAM.[112] However, while sulfide-based SSEs offer greater plasticity, their lower hardness and fracture toughness can lead to the formation of brittle cracks, as noted by McGrogan et al.[113]

The volume expansion and pressure buildup in the In/$Li_{10}GeP_2S_{12}$/$LiCoO_2$ (In/LGPS/LCO) cells have been directly observed by monitoring pressure variations and dilatometric height changes during galvanostatic cycling.[104] XRT revealed bending and cracking at the nonpressurized edges of the SSB,

https://doi.org/10.1021/acsenergylett.4c02476
ACS Energy Lett. 2025, 10, 496−525

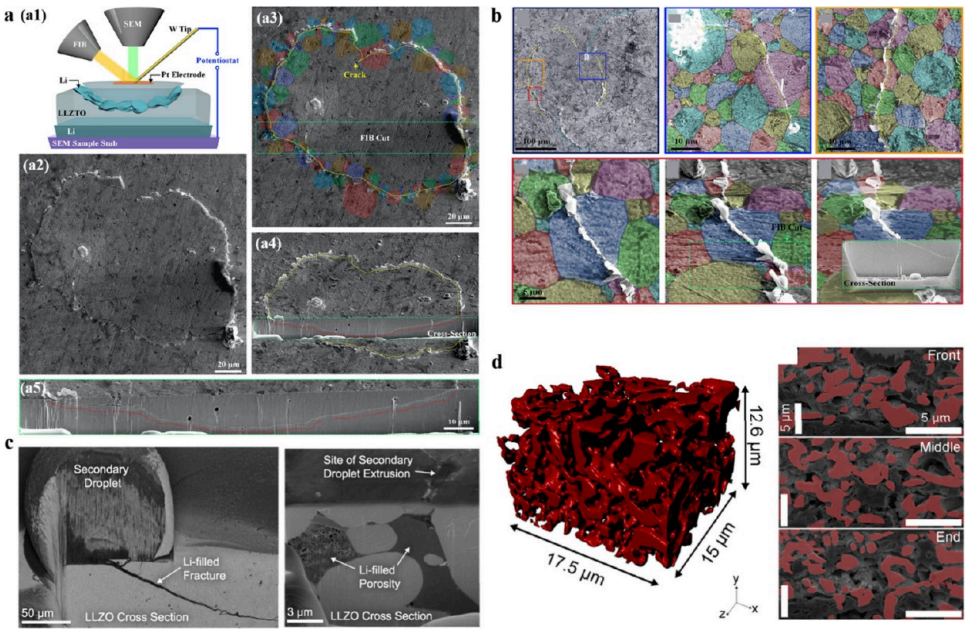

Figure 8. (a1) A schematic showing the *in situ* cell setup and formation of a bowl-shaped crack. (a2, a3) SEM images depicting the formation of a bowl-shaped crack on the surface of the LLZTO. (a4) A cross-sectional view highlighting the bowl-shaped crack, where the yellow and red dotted lines indicate the crack on the top surface and within the cross section, respectively. (a5) A magnified view of the bowl-shaped crack in the cross-sectional region. (b) SEM images showing Li propagation through the LLZTO grains. Reproduced with permission.[123] Copyright 2021, Royal Society of Chemistry. (c) Cross-sectional FIB-SEM images of a secondary Li droplet and pores with filled Li. Reproduced with permission.[124] Copyright 2021, Elsevier. (d) A full 3D tomographic rendering of the porous indium metal and segmented SEM images. Reproduced with permission.[126] Copyright 2020, American Chemical Society.

indicating significant volume expansion and pressure changes (Figure 7a). These pressure variations are primarily attributed to the volumetric expansion of LCO during delithiation within the composite cathode and the volume change associated with the conversion of indium from a tetragonal to a cubic alloy $InLi_{1-x}$ phase. However, interpreting the data is complicated by simultaneous expansion of both the anode and cathode during charging. To isolate the impact of cathode expansion on battery performance, a zero-strain $Li_4Ti_5O_{12}$ (LTO) anode was substituted for Li metal, creating LTO/LGPS/LCO SSBs (Figure 7b). This configuration ensured that pressure changes were solely due to the cathode material. Results showed reduced pressure fluctuations at higher cycling rates, confirming that LCO expansion degrades cell performance. The layered structure of LCO undergoes unit cell expansion during the delithiation process as the removal of Li^+ ions reduces the screening effect on the negatively charged CoO_6 layers, causing lattice expansion along the *c*-axis.[115]

Neumann et al.[114] conducted 3D microstructure simulations using XRT-derived data from β-Li_3PS_4/$Li(Ni_{0.6}Mn_{0.2}Co_{0.2})O_2$ (β-LPS/NMC622) composite cathodes (Figure 7c). Their findings suggest that poor electronic conductivity, due to limited contact area between the NMC and the current collector, leads to a self-accelerating decrease in specific capacity under high-current conditions. Additionally, particle delamination studies showed that high discharge rates cause overpotential and capacity loss due to NMC expansion within the composite cathode, which compresses the electrolyte matrix.[116,117] This generates significant interfacial stress at the reaction sites, limiting Li^+ ion intercalation and potentially fracturing the SSE matrix. During delithiation, the shrinkage of NMC particles causes delamination from the SSE matrix, increasing interfacial resistance and accelerating capacity decay in SSBs.[118,119] These detrimental effects are common in conventional cathode materials.

In contrast to layered cathodes, conversion-type cathodes, like copper sulfide (CuS), with a high theoretical capacity density of up to 561 mAh g^{-1}, have been widely studied.[120−122] Zhang et al. investigated CuS/β-Li_3PS_4/Li SSB and identified phase transformations and crack formation within the CuS cathode particles.[40] They found micrometer-sized Cu inclusions, indicative of phase evolution within the CAMs. XRT analysis showed the cracks predominantly aligned in the $x-y$ plane, perpendicular to the applied pressure (Figure 7d,e). Importantly, increasing the stack pressure from 26 to 40 MPa was shown to suppress crack formation, demonstrating that mechanical optimization can mitigate these issues.

In summary, localized and buried interfaces pose significant challenges to the development of ASSBs. Advanced XRT techniques provide invaluable insights into the morphological and structural changes in Li anodes, SSEs, and composite cathodes. XRT enables intuitive visualization of buried structures, such as voids, cracks, Li dendrites, and newly formed interphases, all of which contribute to battery degradation. While XRT is a powerful tool for examining ubiquitous interfaces, it has limitations. XRT is not well-suited to determining the phase distribution of individual components in composite cathodes, a key factor in interfacial reactions. XRT also struggles with distinguishing the morphology of metallic Li from the surrounding ceramic materials with high-Z elements due to limited resolution and the low phase contrast of low-Z materials. In contrast, FIB-SEM, combined with elemental mapping (via energy-dispersive spectroscopy or EDS), can effectively address these challenges. It offers higher resolution and provides detailed phase distribution information, making it an invaluable tool for investigating the chemical and structural

https://doi.org/10.1021/acsenergylett.4c02476
ACS Energy Lett. 2025, 10, 496−525

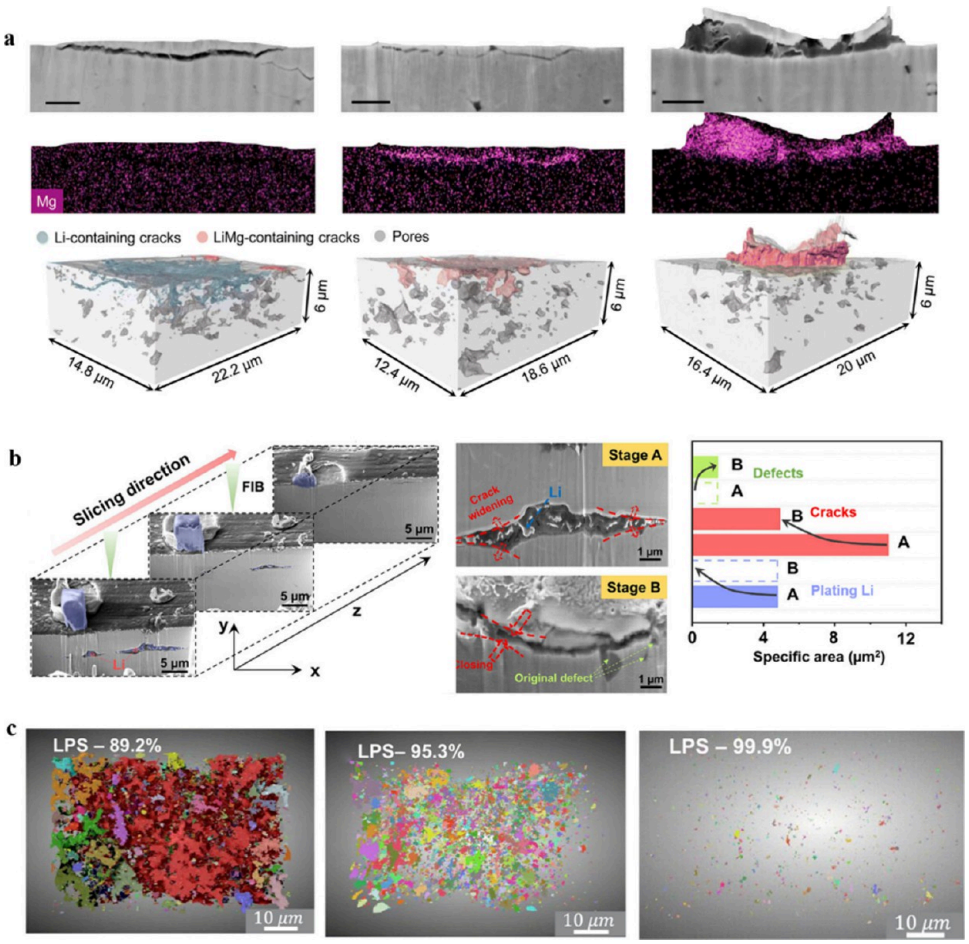

Figure 9. (a) Cross-sectional FIB-SEM and EDS images of the evolution of spallation cracks at three different cycled stages of LiMg/LLZTO/Li ASSBs and 3D demonstrations of the surface cracks on the LLZTO surface. Reproduced with permission.[128] Available under CC BY 3.0. Copyright 2024, Royal Society of Chemistry. (b) The FIB-SEM depth profiles of Li filament inside the LLZTO SSE after plating and quantitative analysis of the region of cracks, Li filaments, and defects in the SSEs. Reproduced with permission.[129] Copyright 2024, American Chemical Society. (c) 3D rendering structure of pores networks inside the LPS pellets at relative densities of 89.2%, 95.3%, and 99.9%, respectively. Reproduced with permission.[130] Available under a CC BY 4.0. Copyright 2024, Springer Nature.

evolution of ASSBs. Notably, FIB-SEM can realize a spatial resolution of greater than 1 nm, effectively bridging the gap between XRT (>10 nm) and NI (>10 μm). The integration of these methods offers crucial insights into the morphological, structural, and compositional evolution of the interfaces in ASSBs, spanning scales from the micro- to nanometer range.

Recent Progress in Focused Ion Beam Scanning Electron Microscopy. FIB-SEM can reach spatial resolution in the nanometer range, enabling detailed investigations of local microstructure transformation, elemental mapping (EDS), etc. Additionally, the high vacuum environment ($\sim 10^{-3}$ Pa) required for FIB-SEM testing is well suited to the study of SSEs that are sensitive to air. Furthermore, FIB-SEM enables both surface imaging (SEM mode) and depth imaging through the sample, making it possible to unveil the 3D localized and buried information on the batteries. This section primarily summarizes research progress concerning the FIB-SEM technique and their associated application in ASSBs, encompassing dendrite growth along the SSEs and the formation of cracks within both cathode particles and SSEs.

Li/SSE Interface. Segmenting Li, cracks, and pores within SSEs presents significant challenges due to their buried nature. To address this, advanced FIB tomography techniques have been employed to observe these substances on the nanoscale. Using FIB-SEM (Figure 8a1), Zhao et al.[123] investigated the mechanisms of Li deposition and its correlation with crack formation in garnet LLZTO. Their observations revealed the formation of a fine line crack with a closed-loop profile on the upper surface of the LLZTO (Figure 8a2–a4). During electrochemical cycling, Li metal emerged along the crack line, eventually extruding onto the surface of the LLZTO (Figure 8a2). As the Li extrusion continued, the crack line progressively widened, leading to the formation of a Li metal ring on the surface (Figure 8a2–a4). To further investigate the depth and structure of these surface cracks, the authors used FIB to mill a trench perpendicular to the LLZTO surface (Figure 8a4,a5). Notably, they identified a reproducible "bowl-shape" crack beneath the Pt electrode (Figure 8a4,a5), illustrating the 3D near-surface crack geometry. Their findings suggest that Li predominantly propagates along transcrystalline cracks in LLZTO (Figure 8b). These cracks appear to originate within the interior of the LLZTO, below the electrode surface, and propagate outward in a curved trajectory toward the surface. The resulting bowl-shaped cracks resemble hydraulic fractures caused by high fluid pressure on the internal crack surfaces, indicating that the pressure generated by Li deposition is the primary driver of crack initiation and propagation. This hypothesis is further supported by the observation that Li

https://doi.org/10.1021/acsenergylett.4c02476
ACS Energy Lett. 2025, 10, 496–525

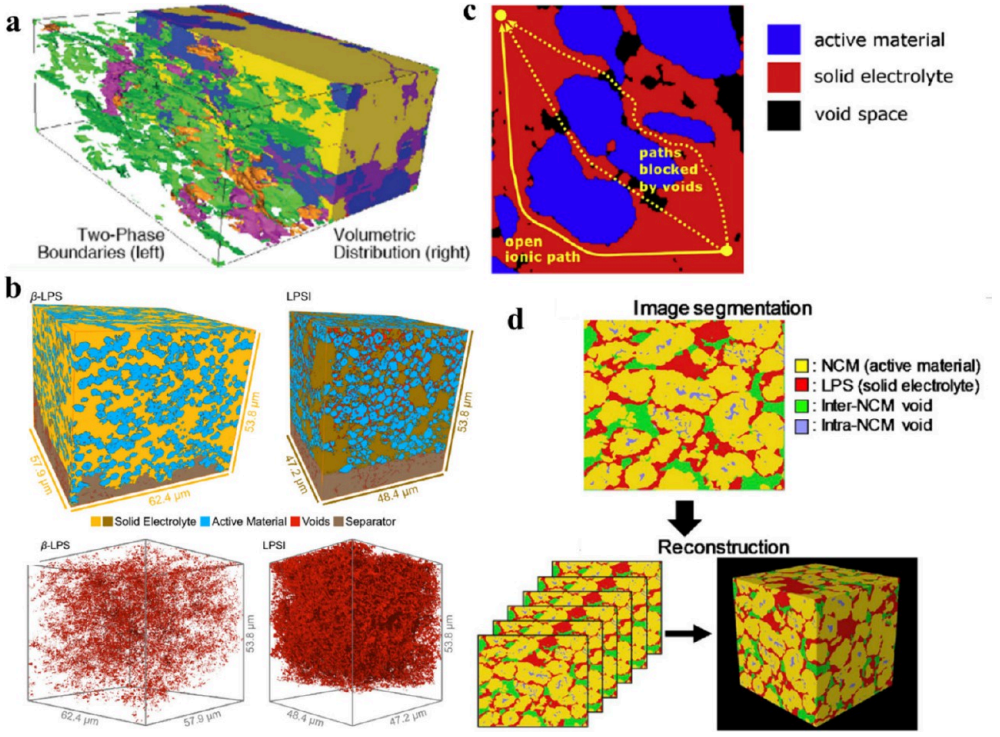

Figure 10. (a) Quantitative microstructure analysis of the $(Li_2S)_8(P_2S_5)_2(Ni_3S_2)_1/LiNi_{0.6}Co_{0.2}Mn_{0.2}O_2$ composite cathode in ASSBs. Reproduced with permission.[134] Copyright 2018, American Chemical Society. (b) The visualization of the two reconstructed NMC cathodes, with β-LPS and LPSI as solid electrolytes and the corresponding spatial distribution of voids in the β-LPS and LPSI sample. Reproduced with permission.[135] Copyright 2021, Elsevier. (c) An image that combines the reconstructed phases of LCO particles (blue), SSE (red), and void space (black), where SSE represents the volume not occupied by LCO or void phase. Reproduced with permission.[136] Copyright 2018, Elsevier. (d) Quantitative analytical procedure for the 3D structural properties of composite cathodes in SSBs. Reproduced with permission.[137] Copyright 2020, Elsevier.

flowed between the crack flanks, leading to crack widening and expansion as lithium deposition continued.

The inherent mechanical properties of the Li metal are also critical to the performance of ASSBs. The mechanisms of Li penetration in molten Li/LLZO system were elucidated by Bryan et al.[124] using an in-plane cell configuration (Figure 8c). As the current density increased, secondary Li droplets were extruded from the surface of LLZO near the plated electrodes. Their findings demonstrated that molten Li propagation involves cycles of pressure buildup and release, allowing pressure relaxation within the Li anode. This mechanism helps to prevent LLZO fracture and Li filament formation, resulting in a significant increase in the CCD near the melting point of Li. Notably, this CCD was an order of magnitude higher than that of solid Li, owing to the altered mechanical properties of molten Li. Similarly, Kazyak et al.,[125] utilizing an in-plane cell visualization setup, showed that Li stripping from the solid Li anode creates voids, while the plated side maintains intimate contact between the solid Li electrode and LLZO SSEs at the interface. These voids were identified as the primary cause of the increased interfacial impedance, hindering charge transfer kinetics.

By chemically dealloying the Li–In alloy in dry methanol, researchers constructed a porous In metal anode (Figure 8d), which effectively accommodated the volume expansion associated with electrochemical lithiation and delithiation.[126] This strategy mitigated chemo-mechanical failure while maintaining a continuous electrically and ionically conductive network. Notably, the cycling stability of the porous In anode was significantly better than that of dense In in ASSBs, showing great promise for the use of porous metals in these systems.[126] Moreover, appropriate external pressure and interfacial optimization strategies have proven effective in enhancing electro-chemo-mechanical interactions.[127] The applied pressure directly influences the CCD and the growth of Li dendrites. It is important to note that external pressure plays a significant role in the performance of ASSBs. Additionally, optimizing the interface between the Li electrode and the SSE is critical for accelerating the commercial development of ASSBs.

Li Penetration within SSEs. Recent observations suggest that Li metal can plate within SSEs as a result of electric current leakage in hidden pores or along grain boundaries.[131−133] Siniscalchi et al.[128] provided direct experimental evidence using FIB tomography, showing Li deposition on both the surface and subsurface of LLZTO after Li plating. In their study, magnesium (Mg) was used as a tracer element, confirming that pure Li metal could electroplate in isolated subsurface pores. This led to pressure buildup, which ultimately triggered the initiation of dendrites, as displayed in Figure 9a. This investigation provides critical insights into the relationship between isolated Li deposition and the nucleation of Li dendrites, thereby advancing our understanding of the recently proposed mechanism of dendritic initiation in SSEs.[84] The evolution of isolated Li dendrites within SSEs, a key aspect of the dendritic propagation process, was recently explored by Cao et al.[129] Their findings revealed that Li filaments grow within LLZTO but may unexpectedly self-dissolve (stage A-B in Figure 9b) when the current density decreases, even without reversing the current direction. However, despite the dissolution of Li filaments, the resulting cracks significantly reduce the mechanical strength of

https://doi.org/10.1021/acsenergylett.4c02476
ACS Energy Lett. 2025, 10, 496−525

the SSE. Additionally, through a coupled electro-chemo-mechanical model, the authors demonstrated that filament growth is strongly influenced by the competition between the electrochemical driving force and the mechanical resistive force.

These studies underscore that Li penetration in SSBs is intricately linked to several factors, including the mechanical properties of Li, nonuniform plating at the Li/SSE interface, interlayer optimization, and microstructural defects on the surface and subsurface of the SSE. However, there is still no consensus on the failure mechanisms across different SSE materials. Diallo et al.[130] proposed four failure mechanisms due to Li dendrite growth by studying the microstructural characteristics of 75%Li_2S-25%P_2S_5 (LPS) with varying relative densities (Figure 9c). The first failure mechanism involves the propagation of Li filaments through a network of percolating pores, driven by the low overpotential required for filament growth, which is particularly prevalent in SSE pellets that do not reach the critical density threshold (>95%). The second mechanism involves the chemical instability between the SSE material and Li, leading to the formation of SEI. While this chemical reaction is relatively limited in the current LPS system due to the rapid stabilization of the SEI layer, it remains a significant factor in other SSB systems. The third mechanism concerns the electronic conductivity of the SSEs, which facilitates isolated Li deposition in pores, eventually leading to short circuits as these pores become interconnected. This effect is minimized in the presence of percolating pores. Lastly, the fourth mechanism is related to the fracture of the SSE under high current densities, particularly when the material has low fracture toughness. This failure mode is most frequently observed in dense SSE pellets without percolating pores at elevated current densities.

These four mechanisms are often intertwined, and it is crucial to note that the first mechanism (percolating pores) is highly dependent on the microstructure of the SSE pellets, whereas the other three mechanisms are influenced by the intrinsic material properties of the SSE itself. Therefore, these findings are not limited to sulfide-based systems. The critical density threshold (~95% for LPS) identified for mitigating percolating pore formation is likely applicable to other SSE materials as well.

Cathode Active Materials (CAMs)/SSEs Interface. Solid-state composite cathodes have more complex structural features and differ significantly from a conventional liquid electrolyte-based cathode. The FIB analysis technique is expected to reveal the phase distribution of individual components in composite cathodes and to provide quantitative information associated with the microstructure of each component, such as volume, pore, connectivity, and tortuosity.[134] In addition, the effective reaction sites, i.e., the active interfaces formed by each component, can be precisely confirmed through a 3D reconstructed structure (Figure 10a). Kroll et al. elucidated the impact of morphology and ionic conductivity of the small mesoporous β-Li_3PS_4 and large nonporous Li_3PS_4·LiI (LPSI) on ASSB performance using FIB.[135] Specifically, the shape of the SSEs affects the microstructure of the composite cathodes and, in particular, has a significant effect on Li-ion transport pathways within the electrode, the actual contact area between the active materials (NMC) and SSEs, and the distribution of (undesirable) voids (Figure 10b). Although LPSI has a high ionic conductivity, it still cannot avoid the performance degradation due to increased ion transport tortuosity caused by the large SSE particle size and undesirable voids. This study revealed the importance of qualitative and quantitative analysis of morphological features, which enable understanding of kinetic limitations in ASSBs. In order to analyze the effect of composite cathode microstructure on the ionic transport properties, Hlushkou et al.[136] used both impedance spectroscopy measurements and numerical simulations based on reconstructed microstructures to obtain ion transport tortuosity values, respectively. The authors proposed that the voids in the composite electrode exerted a significant influence on the ion transport path (Figure 10c), and therefore, a low volume fraction is the key to achieving efficient ASSBs. To optimize interfacial contact area between NCM and LPS, Nakamura et al.[137] presented a dry coating strategy to produce an NMC@LPS core−shell composite particle. This electrode structure (Figure 10d) achieves a well-percolated ion transport pathway, significantly improving the rate capability and cycle performance of the ASSBs.

In summary, FIB-SEM, combined with elemental mapping through EDS, effectively addresses the challenges in unveiling chemical reactions within ASSBs. Advanced FIB-SEM techniques provide a higher resolution and detailed phase distribution information. This makes it an invaluable tool for investigating the chemical and structural evolution of ASSBs.

While advanced FIB-SEM techniques have proven highly effective in capturing the structural and morphological evolution of the Li anode, SSEs, cathode, and their interfaces within ASSBs, they fall short in providing localized chemical information at the atomic scale.[138] Fortunately, Cryo-TEM techniques can significantly realize chemical and structural characterization of Li metal and interphase at the atomic level, effectively bridging the gap between FIB-SEM (>1 nm) and XRT (>10 nm) and spanning scales from the nanometer to atom range.

Recent Progress in Cryogenic Transmission Electron Microscopy (Cryo-TEM). TEM is distinguished by its exceptional high-resolution visualization capabilities.[43] However, its application in studying Li metal and its SEI is significantly limited by the thermal instability of Li and its sensitivity to electron beam irradiation. Cryo-TEM, initially utilized in structural biology, presents a promising solution. By operating at cryogenic temperatures, cryo-TEM significantly reduces beam-induced damage, making it indispensable for atomic-level characterization of Li metal. Recently integrated into battery research, cryo-TEM demonstrates exceptional capability in preserving and investigating Li metal structurally and chemically.[44,139,140] The application of cryo-TEM in battery research is centered around two main areas: visualization of the SEI and CEI, and elucidation of the chemistry of the Li/SSE interface at the atomic scale.

SEI and CEI Chemistry of ASSBs. The composition−property−function relationship of SEI in liquid LIBs has been extensively investigated over the last four decades, as the SEI is believed to be the key to the performance, safety, and cycle life of the battery.[141−143] Two widely accepted models of SEI, the mosaic SEI and the multilayer SEI, were established by Peled et al.[144] and Aurbach et al.,[145] respectively. These models serve to elucidate the structural and chemical transformation mechanisms within the SEI. Compared to their liquid electrolyte counterparts, most SSEs exhibit thermodynamic instability when in contact with Li metal. This instability leads to the formation of a complex interphase, similar to the SEI observed in liquid electrolyte systems. The possibility of SSEs to develop SEI when in contact with Li metal has been theoretically predicted for various conventional SSEs, including LLZO, LGPS, LPS, and

https://doi.org/10.1021/acsenergylett.4c02476
ACS Energy Lett. 2025, 10, 496−525

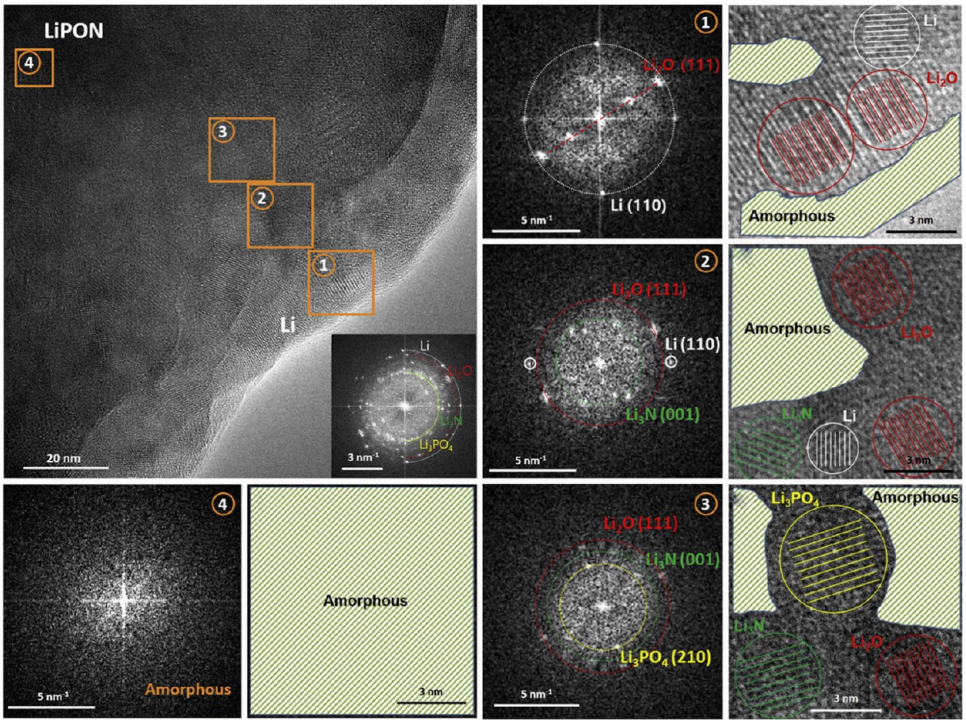

Figure 11. HRTEM images of the Li/LiPON interphase and corresponding fast Fourier transform (FFT) patterns of four marked regions (1−4). Reproduced with permission.[139] Copyright 2020, Elsevier.

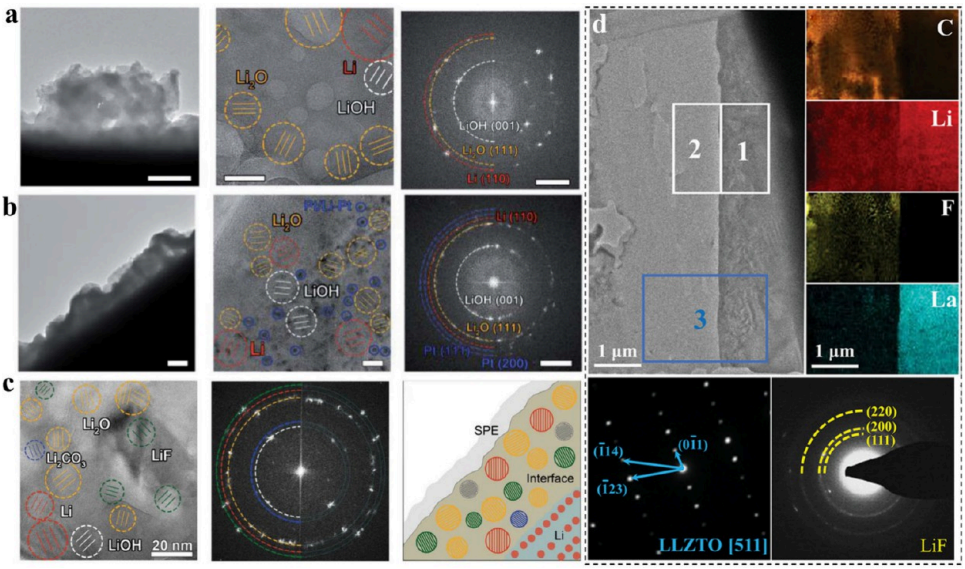

Figure 12. (a) TEM images of the SPE electrolyte interface without sputtering Pt after Li deposition and corresponding HRTEM image of interface contained crystalline Li, Li_2O, LiOH, and an amorphous component. Reproduced with permission.[153] Copyright 2020, The Royal Society of Chemistry. (b) SPE electrolyte interface with 5 nm sputtered Pt after Li deposition and HRTEM image of interface contained crystalline Li, Li_2O, LiOH, Pt, and amorphous solid polymer electrolytes. Reproduced with permission.[153] Copyright 2020, The Royal Society of Chemistry. (c) The crystalline particles include Li_2O, Li_2CO_3, and LiOH in the Li metal interface, the corresponding FFT and schematic demonstration of the mosaic structure corresponding to the identified interface. Reproduced with permission.[154] Copyright 2020, Wiley-VCH GmbH. (d) Cryo-TEM results of the Li/LLZTO interface and the corresponding elemental mapping distribution results and EDPs results for regions 1 and 2. Reproduced with permission.[157] Copyright 2022, Wiley-VCH GmbH.

amorphous Li phosphine oxynitride (LiPON), and subsequently validated through experimental findings.[85,146−148] Despite considerable research efforts focused on the evolution of the Li/SSE interface, the formation mechanism of the SEI in ASSBs remains elusive.

Motivated by the impressive electrochemical performance of thin-film LiPON solid batteries, Cheng et al.[139] adopted cryo-TEM techniques to explore the characteristics of the stable Li/LiPON interphase. Their observations revealed a dense 76 nm-thick interphase composed of Li_2O, Li_3N, and Li_3PO_4. This finding suggests a multilayer mosaic SEI structure characterized

https://doi.org/10.1021/acsenergylett.4c02476
ACS Energy Lett. 2025, 10, 496−525

by concentration gradients of nitrogen (N) and phosphorus (P) within an amorphous matrix (Figure 11). Such a thin interphase, with a gradient structure of ion-conducting but electron-insulating components, can impede further decomposition of the SSEs due to the presence of equilibrium phases such as Li_2O, Li_3N, and Li_3PO_4. However, this passivation effect cannot be achieved when the decomposition products are MCI. For instance, the reduction of compounds like $Li_{10}GeP_2S_{12}$ and $Li_{0.5}La_{0.5}TiO_3$ by Li metal yields a conductive Li−Ge alloy and a titanate interfacial phase, which fails to mitigate successive decompositions.[149] In terms of the composition of successful SEI in liquid batteries, the main components within the SEIs include alkyl Li species, LiF, Li_2O, and Li_2CO_3. Among these, LiF stands out as a favored SEI component due to its lower electronic conductivity and higher thermodynamic stability to Li metal, thereby exerting a passivating effect.

Meng's research group used $LiNi_{0.5}Mn_{1.5}O_4$/LiPON/Li (LNMO/LiPON/Li) thin-film full cells to investigate the chemistry of CEI and understand the origin of a stable interphase existing between the LNMO and LiPON interface.[150] Remarkably, the LNMO/LiPON interface maintained intimate contact without exhibiting voids or cracks, even after 500 cycles. In addition, there is a significant difference between the crystalline and amorphous domains of the LNMO/LiPON interface in the cryo-TEM images, and these studies provide evidence of the long-term structural stability of the LNMO/LiPON interface. The stability of the LNMO/LiPON interface can be ascribed to the inherent structural resilience of LNMO and LiPON. An artificial deposition of LiPON layers on the cathode surface is regarded as a straightforward protection strategy to mitigate the interfacial reactions between the electrochemically less stable SSEs and the highly oxidative cathode material. These stable interphases observed at Li/LiPON and LNMO/LiPON interfaces offer invaluable insights for further investigation of other SSE interphases in ASSB systems.

Atomic-Scale Li/SSE Interfacial Chemistry. Only a few battery systems can achieve the same excellent electrochemical performance as LiPON thin-film batteries. Interface issues between SSEs and Li anodes remain an obstacle to the development of ASSBs. In the case of poly(ethylene oxide) (PEO) electrolytes containing $LiN(SO_2CF_3)_2$ (LiTFSI) salts, contact with Li metal leads to immediate oxidation, generating Li_2O along with H_2 and C_2H_4.[151,152] This reaction, coupled with the repeated interaction of fresh solid polymer electrolyte (SPE) with Li, results in thickening of the Li/PEO interface, leading to high electrochemical impedance and uneven surface morphology.

The cryo-TEM technique enabled the atomic-scale observation of Li anode and its interfacial structures in SPEs. Sheng et al.[153] found that the deposited Li grew rapidly at the Li/PEO interface, forming a blocky, porous structure as displayed in Figure 12a. Through further examination of the Li/PEO interface, they unveiled a mosaic structure at the atomic scale, with Li, LiOH, Li_2O, and Li_2CO_3 crystalline grains dispersed within the amorphous phase (Figure 12c).[154] Additionally, Li metal close to PEO tends to form polycrystalline particles rather than single crystalline Li. This observation suggests violent side reactions between Li metal and PEO, compromising interfacial contact and recyclability. Consequently, efforts to stabilize ASSBs have focused on modifying the Li/PEO interface guided by cryo-TEM visualization.

Leveraging the superior ionic/electronic conductivity of lithium−platinum (Li−Pt) alloys[155,156] (Li_5Pt, Li_2Pt, *etc.*), Tao's group introduced a thin Pt nanointerlayer between the Li anode and PEO-based electrolyte.[153] Cryo-TEM analysis confirmed the formation of amorphous Li−Pt alloy nanoparticles at the Li/PEO interface (Figure 12b), reducing interfacial impedance and enhancing ionic/electronic conductivity. As a result, a more homogeneous and dense Li deposition at the interface is obtained.[153] Furthermore, the introduction of a Li_2S additive facilitated the decomposition of $N(CF_3SO_2)_2^-$ ($TFSI^-$) and promoted the formation of LiF nanocrystals at the Li/PEO interface, which prevents C−O bond breakage and enhances cyclability and stability.

Similarly, Dai et al.[157] developed a LiF-rich interlayer at the Li/LLZTO interface to enhance the ASSB performance. An interlayer (Figure 12d) was formed in situ through a conversion reaction between high-temperature molten Li and thin fluorinated graphite (CF_x) to improve the Li/LLZTO interface. Cryo-TEM analysis revealed the presence of LiF nanocrystals within an amorphous carbon matrix, facilitating homogeneous Li-ion transport and preventing dendrite growth in LLZTO. This complex structure of amorphous carbon and LiF governs the homogeneous transport of Li^+ ions at the Li/LLZTO interface, preventing the growth of Li dendrites in LLZTO, thus improving the CCD and the electrochemical stability of ASSBs.

In addition, to gain insights into the evolution and failure mechanisms of the sensitive Li/sulfide electrolyte interface, Guo et al.[158] employed cryo-TEM measurement to provide atomic-scale chemical and structural information regarding the Li/Li_4SnS_4 (Li/LSS) interface. Following Li deposition, porous lumpy Li formations were observed, analogous to those found at the Li/PEO interface.[153] This undesirable Li deposition is attributed to the side reactions occurring between Li and the LSS electrolyte. A mosaic structure of randomly dispersed Li_2S and Sn_2S_3 crystals is directly identified at the interface by high-resolution TEM, which correlates with the appearance of an interfacial adverse reaction ($2Li + 2Li_4SnS_4 = 5Li_2S + Sn_2S_3$) at the Li/LSS interface. This continuous growth of the unstable interface leads to an increase in the Li^+ ion conduction barrier, which, together with the subsequent preferential deposition of Li along the interfacial conductive byproducts to the GD of the bulk electrolyte, results in rapid depletion of the active Li source and cell failure.

SUMMARY AND OUTLOOK

This review highlights the fundamentals and workflows of the state-of-the-art imaging techniques and their associated applications (Figure 13), shedding light on the buried and widespread interfacial evolution within solid-state electrodes and elucidating critical working and failure mechanisms in all-solid-state batteries (ASSBs). We summarized and detailed recent advancements in neutron imaging (NI), X-ray tomography (XRT), focused ion beam scanning electron microscopes (FIB-SEM), and cryogenic transmission electron microscopy (cryo-TEM), discussing their capabilities, limitations, and potential for further development and effective implementation.

A comparative analysis of these imaging techniques, presented in Table 3, underscores the advantages of synchrotron-based NI and XRT in enabling operando research. These methods complement each other in studying ASSBs. NI excels in penetrating deep into thick materials and detecting lithium-ion transport and distribution in solid state electrolytes (SSEs), though its current limitations include lower spatial resolution

https://doi.org/10.1021/acsenergylett.4c02476
ACS Energy Lett. 2025, 10, 496−525

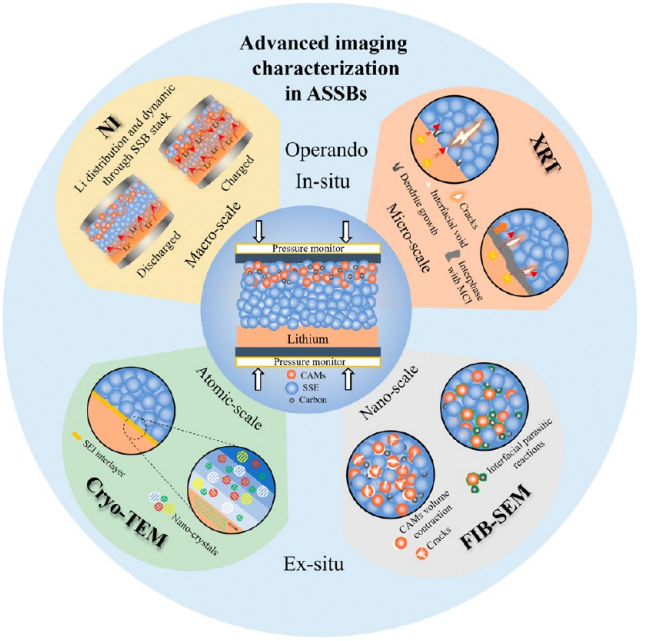

Figure 13. Summary of the state-of-art imaging characterization techniques used in ASSBs.

(>10 μm) and higher costs. XRT provides two-dimensional/three-dimensional (2D/3D) and four-dimensional (4D, i.e., 3D plus time) insights into the structural and morphological evolution of battery materials, making it ideal for nondestructive micro- and mesoscale studies. Integrating these two techniques with advanced data analysis will offer a more comprehensive understanding of ASSBs, which will drive innovation and enhance both battery performance and safety. However, application of these two techniques in solid-state electrochemistry necessitates further refinement, particularly in achieving high temporal resolution to capture instantaneous phase changes during charge/discharge cycles. The forthcoming fourth generation of synchrotron light sources holds promise for enhancing temporal resolution and enabling transient detection, thereby driving advancements in materials science and energy storage.

During *operando* measurements, successive and massive 3D image data sets can be generated, necessitating automated batch processing for efficient analysis. Tomographic artifacts caused by beam damage also pose challenges, requiring complementary tools such as artificial intelligence (AI) for processing NI and XRT results and advancing SSB research.[19,56,159,160] Segmenting tomographic images of cell characterization is a critical step that significantly affects the outcomes of materials characterization and electrochemical simulations. However, manually labeling large *operando* data sets from synchrotron facilities is time-consuming, and these data sets are often difficult to segment using traditional histogram-based methods.[161,162] In such cases, machine learning provides a robust solution by leveraging large data sets from *in situ*/*operando* experiments, significantly improving the efficiency and accuracy of data processing.[163−165] For instance, Liu et al.[166] introduced a deep learning-based approach for image jitter correction, improving tomographic reconstructions quality. Similarly, Su et al.[162] proposed a convolutional neural network-based approach to achieve high accuracy with minimal labeled data, predicting volumes of billions of voxels in mere minutes. Beyond imaging, machine

Table 3. Comparison of Four Different Imaging Techniques

Scale resolution	Imaging techniques	Spatial resolution	Advantages	Limitations	Imaging information
Macroscopic scales	NI	>10 μm	Nondestructive; 3D information; in situ and operando experiment; deep penetration; sensitive to isotope and light elements	Limited spatial resolution; longer exposure times; radiation safety concerns	3D visualization; Li gradient distribution of the cell; elemental and isotopic composition; mechanical and structural changes
Micro- and mesoscopic scales	XRT	>10 nm	Nondestructive; 3D information; in situ and operando experiment; rapid imaging	Low spatial resolution; contrast limitations; special cell design; high threshold for data analysis	3D structure; structural and morphology evolution information of electrode and interface
Atomic and nanoscale	FIB-SEM	>1 nm	High spatial resolution; 3D imaging; adjustable magnification; ability to install accessories	Destructive; difficult transfer sample; local information of sample	Surface; depth information; elemental mapping
	Cryo-TEM	>0.01 nm	Atomic resolution; suitable for sensitive energy materials; elemental analysis	High requirement and cost for sample preparation; not applicable for in situ/operando experiments	Surface/lattice; structure and composition of crystalline particles and SEI

https://doi.org/10.1021/acsenergylett.4c02476
ACS Energy Lett. 2025, 10, 496−525

learning is increasingly recognized as a critical modeling tool in the field of energy storage. It holds significant potential for accurately determining key battery metrics, such as the state of charge, state of health, and remaining lifetime.[167] We expect that machine learning will drive significant advances in the emerging field of ASSBs.

Advances in battery research require a deeper understanding of the mobility of electrons and ions, incorporating insights from materials science, physics, and chemistry. These multi-scale approaches enable us to connect atomic, particle, and electrode-level processes, offering a complete picture of the bulk reactions occurring within ASSBs and driving future innovations in energy storage.

At the atomic and nanoscale levels, FIB-SEM and cryo-TEM techniques offer novel perspectives on investigating the interfacial reaction dynamics in ASSBs. Although these methods require post-mortem characterization due to their destructive nature, they provide invaluable insights into the intrinsic mechanisms of battery materials. For FIB-SEM that usually employs Ga ion to uncover the inner structure of the specimen, beam damage could exist especially when high milling current is used and/or beam-sensitive specimen is used, such as a lithium anode. In these cases, FIB milling parameter should be optimized, or FIB-SEM equipped with cryogenic sample environment (i.e., cryo-FIB) may be adopted.[168] Cryo-TEM preserves lithium metal in its native state, enabling the study of localized nano- and microstructures and guiding the construction of stable solid-electrolyte interfaces (SEIs). Moreover, advancements in cryo-electron microscopy, inspired by biological research, hold great potential for achieving high-resolution imaging of battery materials in their native state, allowing for a comprehensive investigation of atomic-level chemistry and structure. With that said, to ensure "real" SEI and nanoscale information is unraveled, attention should still be given during the whole workflow from TEM sample preparation and sample transfer to image data acquiring and data analysis.[169,170]

As discussed in this review, various imaging techniques have been applied to cutting-edge research areas in ASSBs, yielding significant discoveries and insights into different scientific case studies. While these methods have been independently validated, each has its own advantages and limitations. Their effective integration holds the potential to unlock unprecedented scientific opportunities. While certain modalities can be combined within a single terminal station, others must be performed sequentially due to physical constraints. A comprehensive yet tailored experimental design is, therefore, essential for each case study. Feasible strategies could be that nondestructive imaging techniques like NI and XRT are first conducted under *in situ* or *operando* conditions with 3D imaging data sets acquired together with electrochemical performance, followed by characterization like FIB-SEM and TEM that is destructive or usually post-mortem analysis. *In situ* and *operando* cells are crucial to acquire reliable and desired data sets. Relevant cell designs have been well summarized in reviews[47,171] where readers are directed. Note that for image reconstruction, several open-source algorithms are available, like Tomopy, ASTRA Toolbox, PyHST2, and so on. While for image process and analysis, free software like ImageJ (or Fiji) and 3D Slicer are good options for 2D and 3D image analysis, respectively. In addition, commercial software like Avizo, VGStudio, and Dragonfly offer platforms that integrate basic and advanced functions, including image processing, 3D visualization, 2D/3D analysis, and so on. With these tools available, challenges still exist on how to integrate and analyze multimodel imaging data sets across multiscale, to comprehensively unravel the electro-chemo-mechanical interplay and the degradation and failure mechanisms. This necessitates multidisciplinary input and the teamwork of experts from material/chemistry, characterization techniques, and image analysis.

One of the critical challenges for ASSBs moving forward is optimizing the stack pressure. Future research should focus on refining pressure regulation techniques to maintain an optimal balance, avoiding both void formation and mechanical stress-induced failures. Additionally, exploring the effects of stack pressure across a wider range of SSE materials will be vital in generalizing findings beyond specific systems, such as oxide-type SSEs. As our understanding of electro-chemo-mechanical interactions in ASSBs deepens, advancements in interfacial engineering and pressure management will be essential for extending battery life and improving performance under high charge/discharge rates.

In summary, the integration of advanced imaging characterization techniques has propelled the development of battery materials, offering insights into complex electro-chemo-mechanical mechanisms in ASSBs. These multiscale approaches, ranging from atomic to electrode levels, provide a holistic perspective on bulk reactions, facilitating the engineering and advancement of ASSBs. They help answer a range of questions, such as the following: What changes in chemistry and structure govern the bulk reaction in ASSBs, including those involving Li, SSEs, and cathodes? How do Li transformations propagate within the SSEs? How do interfacial reactions evolve across the electrode architecture? At the atomic level, cryo-TEM provides invaluable insight into the fundamental transformations occurring at the Li/SSEs (SEIs) and cathode/SSEs (CEIs) interfaces. On the particle level, chemical mapping—achievable through advanced techniques like FIB-SEM—offers critical information on how lithium transformations propagate within SSEs. At the electrode level, NI and XRT are indispensable for providing an intuitive, comprehensive view of the structural changes occurring during battery operation. Advances in battery research require a deeper understanding of the mobility of electrons and ions, incorporating insights from materials science, physics, and chemistry. These multiscale approaches enable us to connect atomic, particle, and electrode-level processes, offering a complete picture of the bulk reactions occurring within ASSBs and driving future innovations in energy storage.

AUTHOR INFORMATION

Corresponding Authors

Zhenjiang Yu − *Department of Chemistry, Lancaster University, Lancaster LA1 4YB, United Kingdom;* orcid.org/0000-0002-5572-0377; Email: z.yu10@lancaster.ac.uk

Kang Dong − *Multi-disciplinary Research Division, Institute of High Energy Physics Chinese Academy of Sciences, 100049*

https://doi.org/10.1021/acsenergylett.4c02476
ACS Energy Lett. 2025, 10, 496−525

Beijing, China; orcid.org/0000-0003-4924-2775; Email: dongkang@ihep.ac.cn

Ingo Manke − *Helmholtz-Zentrum Berlin für Materialien und Energie, 14109 Berlin, Germany;* orcid.org/0000-0001-9795-5345; Email: manke@helmholtz-berlin.de

Authors

Xia Zhang − *Helmholtz-Zentrum Berlin für Materialien und Energie, 14109 Berlin, Germany; Electrical Energy Storage Technology, Technische Universität Berlin, 10587 Berlin, Germany*

Markus Osenberg − *Helmholtz-Zentrum Berlin für Materialien und Energie, 14109 Berlin, Germany*

Ralf F. Ziesche − *Helmholtz-Zentrum Berlin für Materialien und Energie, 14109 Berlin, Germany*

Julia Kowal − *Electrical Energy Storage Technology, Technische Universität Berlin, 10587 Berlin, Germany*

Yan Lu − *Helmholtz-Zentrum Berlin für Materialien und Energie, 14109 Berlin, Germany;* orcid.org/0000-0003-3055-0073

Complete contact information is available at: https://pubs.acs.org/10.1021/acsenergylett.4c02476

Notes

The authors declare no competing financial interest.

Biographies

Xia Zhang is a PhD candidate at the Technische Universität Berlin. Her research interests focused on investigating working/degradation mechanism of Li/Na solid-state batteries by nondestructive neutron and synchrotron X-ray imaging techniques.

Markus Osenberg is a materials science researcher known for his expertise in multiscale and operando imaging techniques, particularly in the study of energy materials. His work frequently involves the use of synchrotron X-ray, focused-ion-beam, and neutron imaging, often combined with AI-based methods for data analysis.

Ralf F. Ziesche received his PhD from University College London in 2020, supervised by Prof. Paul R. Shearing. In 2022, he joined Dr. Ingo Manke's Tomography Group at Helmholtz-Zentrum Berlin. His research focuses on developing advanced imaging techniques for characterizing electrochemical devices.

Zhenjiang Yu is a Marie Curie Fellow at Lancaster University. His research focuses on using advanced characterization techniques, such as X-ray imaging and pair distribution function analysis, to study battery failure modes. His research interests include local structural detection, solid-state batteries, and the development of micro- and nanomaterials.

Julia Kowal is Professor of electrical energy storage technology with the Institute for Energy and Automation Technology, TU Berlin. Her research interests include testing, characterization, ageing, modelling, diagnostics, and lifetime prediction of different battery technologies.

Kang Dong is an associate researcher in the Institute of High Energy Physics, Chinese Academy of Sciences. His research interests focus on the working and degradation mechanism of secondary lithium and zinc batteries, particularly based on synchrotron X-ray techniques.

Yan Lu is the head of Institute for Electrochemical Energy Storage at Helmholtz-Zentrum Berlin für Materialien and Energie. She is also full professor at Friedrich Schiller University Jena. Her research focuses on design and synthesis of colloidal particles with tailored mesoscopic structures and their application as energy storage materials.

Ingo Manke is Head of the Tomography Group and Deputy Head of the Institute for Electrochemical Energy Storage at Helmholtz Centre Berlin for Materials and Energy. His particular focus is on the development and application of various different imaging and 3D data analysis techniques in the field of energy materials.

■ ACKNOWLEDGMENTS

This work is sponsored by China Scholarship Council. Parts of the work were supported by the German BMBF funded Röntgen-Angström Cluster project ANISSA (05K22CBA). K.D. would like to acknowledge the Science and Technology Innovation Program of Institute of High Energy Physics, Chinese Academy of Sciences (E4545CU2, E35451U2).

■ REFERENCES

(1) Xu, J.; Zhang, J.; Pollard, T. P.; Li, Q.; Tan, S.; Hou, S.; Wan, H.; Chen, F.; He, H.; Hu, E.; et al. Electrolyte Design for Li-Ion Batteries under Extreme Operating Conditions. *Nature* **2023**, *614* (7949), 694−700.

(2) Harper, G.; Sommerville, R.; Kendrick, E.; Driscoll, L.; Slater, P.; Stolkin, R.; Walton, A.; Christensen, P.; Heidrich, O.; Lambert, S.; et al. Recycling Lithium-Ion Batteries from Electric Vehicles. *Nature* **2019**, *575* (7781), 75−86.

(3) Degen, F.; Winter, M.; Bendig, D.; Tübke, J. Energy Consumption of Current and Future Production of Lithium-Ion and Post Lithium-Ion Battery Cells. *Nat. Energy* **2023**, *8* (11), 1284−1295.

(4) Duffner, F.; Kronemeyer, N.; Tübke, J.; Leker, J.; Winter, M.; Schmuch, R. Post-Lithium-Ion Battery Cell Production and Its Compatibility with Lithium-Ion Cell Production Infrastructure. *Nat. Energy* **2021**, *6* (2), 123−134.

(5) Greim, P.; Solomon, A. A.; Breyer, C. Assessment of Lithium Criticality in the Global Energy Transition and Addressing Policy Gaps in Transportation. *Nat. Commun.* **2020**, *11* (1), 4570.

(6) Chen, R.; Li, Q.; Yu, X.; Chen, L.; Li, H. Approaching Practically Accessible Solid-State Batteries: Stability Issues Related to Solid Electrolytes and Interfaces. *Chem. Rev.* **2020**, *120* (14), 6820−6877.

(7) Liu, J.; Bao, Z.; Cui, Y.; Dufek, E. J.; Goodenough, J. B.; Khalifah, P.; Li, Q.; Liaw, B. Y.; Liu, P.; Manthiram, A.; et al. Pathways for Practical High-Energy Long-Cycling Lithium Metal Batteries. *Nat. Energy* **2019**, *4* (3), 180−186.

(8) Wang, L.; Wu, Z.; Zou, J.; Gao, P.; Niu, X.; Li, H.; Chen, L. Li-Free Cathode Materials for High Energy Density Lithium Batteries. *Joule* **2019**, *3* (9), 2086−2102.

(9) Cho, B.-K.; Jung, S.-Y.; Park, S.-J.; Hyun, J.-H.; Yu, S.-H. In Situ/Operando Imaging Techniques for Next-Generation Battery Analysis. *ACS Energy Lett.* **2024**, *9*, 4068−4092.

(10) Famprikis, T.; Canepa, P.; Dawson, J. A.; Islam, M. S.; Masquelier, C. Fundamentals of Inorganic Solid-State Electrolytes for Batteries. *Nat. Mater.* **2019**, *18* (12), 1278−1291.

(11) Wenzel, S.; Randau, S.; Leichtweiß, T.; Weber, D. A.; Sann, J.; Zeier, W. G.; Janek, J. Direct Observation of the Interfacial Instability of the Fast Ionic Conductor $Li_{10}GeP_2S_{12}$ at the Lithium Metal Anode. *Chem. Mater.* **2016**, *28* (7), 2400−2407.

(12) Xu, L.; Tang, S.; Cheng, Y.; Wang, K.; Liang, J.; Liu, C.; Cao, Y.-C.; Wei, F.; Mai, L. Interfaces in Solid-State Lithium Batteries. *Joule* **2018**, *2* (10), 1991−2015.

(13) Sakuda, A.; Hayashi, A.; Tatsumisago, M. Interfacial Observation between $LiCoO_2$ Electrode and Li_2S-P_2S_5 Solid Electrolytes of All-Solid-State Lithium Secondary Batteries Using Transmission Electron Microscopy. *Chem. Mater.* **2010**, *22* (3), 949−956.

(14) Takada, K.; Ohta, N.; Zhang, L.; Fukuda, K.; Sakaguchi, I.; Ma, R.; Osada, M.; Sasaki, T. Interfacial Modification for High-Power Solid-State Lithium Batteries. *Solid State Ion.* **2008**, *179* (27), 1333−1337.

(15) Jin, T.; Ma, Y.; Xiong, Z.; Fan, X.; Luo, Y.; Hui, Z.; Chen, X.; Yang, Y. Bioinspired, Tree-Root-Like Interfacial Designs for Structural Batteries with Enhanced Mechanical Properties. *Adv. Energy Mater.* **2021**, *11* (25), 2100997.

(16) McDowell, M. T.; Cortes, F. J. Q.; Thenuwara, A. C.; Lewis, J. A. Toward High-Capacity Battery Anode Materials: Chemistry and Mechanics Intertwined. *Chem. Mater.* **2020**, *32* (20), 8755−8771.
(17) Yan, P.; Zheng, J.; Gu, M.; Xiao, J.; Zhang, J.-G.; Wang, C.-M. Intragranular Cracking as a Critical Barrier for High-Voltage Usage of Layer-Structured Cathode for Lithium-Ion Batteries. *Nat. Commun.* **2017**, *8* (1), 14101.
(18) Zhao, Q.; Stalin, S.; Zhao, C.-Z.; Archer, L. A. Designing Solid-State Electrolytes for Safe, Energy-Dense Batteries. *Nat. Rev. Mater.* **2020**, *5* (3), 229−252.
(19) Yang, H.; Tang, P.; Piao, N.; Li, J.; Shan, X.; Tai, K.; Tan, J.; Cheng, H.-M.; Li, F. In-Situ Imaging Techniques for Advanced Battery Development. *Mater. Today* **2022**, *57*, 279−294.
(20) Lou, S.; Yu, Z.; Liu, Q.; Wang, H.; Chen, M.; Wang, J. Multi-Scale Imaging of Solid-State Battery Interfaces: From Atomic Scale to Macroscopic Scale. *Chem.* **2020**, *6* (9), 2199−2218.
(21) Kardjilov, N.; Manke, I.; Woracek, R.; Hilger, A.; Banhart, J. Advances in Neutron Imaging. *Mater. Today* **2018**, *21* (6), 652−672.
(22) Yu, Z.; Shan, H.; Zhong, Y.; Zhang, X.; Hong, G. Leveraging Advanced X-Ray Imaging for Sustainable Battery Design. *ACS Energy Lett.* **2022**, *7* (9), 3151−3176.
(23) Yu, Z.; Wang, J.; Liu, Y. High-Dimensional and High-Resolution X-Ray Tomography for Energy Materials Science. *MRS Bull.* **2020**, *45* (4), 283−289.
(24) Han, B.; Zou, Y.; Xu, G.; Hu, S.; Kang, Y.; Qian, Y.; Wu, J.; Ma, X.; Yao, J.; Li, T.; et al. Additive Stabilization of SEI on Graphite Observed Using Cryo-Electron Microscopy. *Energy Environ. Sci.* **2021**, *14* (9), 4882−4889.
(25) Han, B.; Zou, Y.; Zhang, Z.; Yang, X.; Shi, X.; Meng, H.; Wang, H.; Xu, K.; Deng, Y.; Gu, M. Probing the Na Metal Solid Electrolyte Interphase via Cryo-Transmission Electron Microscopy. *Nat. Commun.* **2021**, *12* (1), 3066.
(26) Huang, W.; Wang, H.; Boyle, D. T.; Li, Y.; Cui, Y. Resolving Nanoscopic and Mesoscopic Heterogeneity of Fluorinated Species in Battery Solid-Electrolyte Interphases by Cryogenic Electron Microscopy. *ACS Energy Lett.* **2020**, *5* (4), 1128−1135.
(27) Li, X.; Ren, Z.; Norouzi Banis, M.; Deng, S.; Zhao, Y.; Sun, Q.; Wang, C.; Yang, X.; Li, W.; Liang, J.; et al. Unravelling the Chemistry and Microstructure Evolution of a Cathodic Interface in Sulfide-Based All-Solid-State Li-Ion Batteries. *ACS Energy Lett.* **2019**, *4* (10), 2480−2488.
(28) Zhang, X.; Wang, S.; Xue, C.; Xin, C.; Lin, Y.; Shen, Y.; Li, L.; Nan, C.-W. Self-Suppression of Lithium Dendrite in All-Solid-State Lithium Metal Batteries with Poly(Vinylidene Difluoride)-Based Solid Electrolytes. *Adv. Mater.* **2019**, *31* (11), 1806082.
(29) Zheng, B.; Liu, X.; Zhu, J.; Zhao, J.; Zhong, G.; Xiang, Y.; Wang, H.; Zhao, W.; Umeshbabu, E.; Wu, Q.-H.; et al. Unraveling (Electro)-Chemical Stability and Interfacial Reactions of $Li_{10}SnP_2S_{12}$ in All-Solid-State Li Batteries. *Nano Energy* **2020**, *67*, 104252.
(30) Kardjilov, N.; Manke, I.; Hilger, A.; Strobl, M.; Banhart, J. Neutron Imaging in Materials Science. *Mater. Today* **2011**, *14* (6), 248−256.
(31) Tengattini, A.; Lenoir, N.; Andò, E.; Viggiani, G. Neutron Imaging for Geomechanics: A Review. *Geomech. Energy Envir.* **2021**, *27*, 100206.
(32) Cao, D.; Zhang, Y.; Ji, T.; Zhu, H. In Operando Neutron Imaging Characterizations of All-Solid-State Batteries. *MRS Bull.* **2023**, *48* (12), 1257−1268.
(33) Magnier, L.; Lecarme, L.; Alloin, F.; Maire, E.; King, A.; Bouchet, R.; Tengattini, A.; Devaux, D. Tomography Imaging of Lithium Electrodeposits Using Neutron, Synchrotron X-Ray, and Laboratory X-Ray Sources: A Comparison. *Front. in Energy Res.* **2021**, *9*, 657712.
(34) Ziesche, R. F.; Kardjilov, N.; Kockelmann, W.; Brett, D. J. L.; Shearing, P. R. Neutron Imaging of Lithium Batteries. *Joule* **2022**, *6* (1), 35−52.
(35) Zhang, Y.; Chandran, K. S. R.; Bilheux, H. Z. Imaging of the Li Spatial Distribution within V_2O_5 Cathode in a Coin Cell by Neutron Computed Tomography. *J. Power Sources* **2018**, *376*, 125−130.
(36) Michalak, B.; Sommer, H.; Mannes, D.; Kaestner, A.; Brezesinski, T.; Janek, J. Gas Evolution in Operating Lithium-Ion Batteries Studied in Situ by Neutron Imaging. *Sci. Rep.* **2015**, *5* (1), 15627.
(37) Siegel, J. B.; Lin, X.; Stefanopoulou, A. G.; Hussey, D. S.; Jacobson, D. L.; Gorsich, D. Neutron Imaging of Lithium Concentration in Lfp Pouch Cell Battery. *J. Electrochem. Soc.* **2011**, *158* (5), A523.
(38) Sun, F.; Gao, R.; Zhou, D.; Osenberg, M.; Dong, K.; Kardjilov, N.; Hilger, A.; Markötter, H.; Bieker, P. M.; Liu, X.; Manke, I. Revealing Hidden Facts of Li Anode in Cycled Lithium-Oxygen Batteries through X-Ray and Neutron Tomography. *ACS Energy Lett.* **2019**, *4* (1), 306−316.
(39) Dong, K.; Markötter, H.; Sun, F.; Hilger, A.; Kardjilov, N.; Banhart, J.; Manke, I. In Situ and Operando Tracking of Microstructure and Volume Evolution of Silicon Electrodes by Using Synchrotron X-Ray Imaging. *ChemSusChem* **2019**, *12* (1), 261−269.
(40) Zhang, Z.; Dong, K.; Mazzio, K. A.; Hilger, A.; Markötter, H.; Wilde, F.; Heinemann, T.; Manke, I.; Adelhelm, P. Phase Transformation and Microstructural Evolution of CuS Electrodes in Solid-State Batteries Probed by in Situ 3D X-Ray Tomography. *Adv. Energy Mater.* **2023**, *13* (2), 2203143.
(41) Pietsch, P.; Wood, V. X-Ray Tomography for Lithium Ion Battery Research: A Practical Guide. *Annu. Rev. Mater. Res.* **2017**, *47* (1), 451−479.
(42) Li, Y.; Huang, W.; Li, Y.; Chiu, W.; Cui, Y. Opportunities for Cryogenic Electron Microscopy in Materials Science and Nanoscience. *ACS Nano* **2020**, *14* (8), 9263−9276.
(43) Liu, Y.; Ju, Z.; Zhang, B.; Wang, Y.; Nai, J.; Liu, T.; Tao, X. Visualizing the Sensitive Lithium with Atomic Precision: Cryogenic Electron Microscopy for Batteries. *Acc. Chem. Res.* **2021**, *54* (9), 2088−2099.
(44) Ju, Z.; Yuan, H.; Sheng, O.; Liu, T.; Nai, J.; Wang, Y.; Liu, Y.; Tao, X. Cryo-Electron Microscopy for Unveiling the Sensitive Battery Materials. *Small Sci.* **2021**, *1* (11), 2100055.
(45) Li, Y.; Huang, W.; Li, Y.; Pei, A.; Boyle, D. T.; Cui, Y. Correlating Structure and Function of Battery Interphases at Atomic Resolution Using Cryoelectron Microscopy. *Joule* **2018**, *2* (10), 2167−2177.
(46) Li, Y.; Li, Y.; Pei, A.; Yan, K.; Sun, Y.; Wu, C.-L.; Joubert, L.-M.; Chin, R.; Koh, A. L.; Yu, Y.; et al. Atomic Structure of Sensitive Battery Materials and Interfaces Revealed by Cryo-Electron Microscopy. *Science* **2017**, *358* (6362), 506−510.
(47) Atkins, D.; Capria, E.; Edström, K.; Famprikis, T.; Grimaud, A.; Jacquet, Q.; Johnson, M.; Matic, A.; Norby, P.; Reichert, H.; et al. Accelerating Battery Characterization Using Neutron and Synchrotron Techniques: Toward a Multi-Modal and Multi-Scale Standardized Experimental Workflow. *Adv. Energy Mater.* **2022**, *12* (17), 2102694.
(48) Bradbury, R.; Dewald, G. F.; Kraft, M. A.; Arlt, T.; Kardjilov, N.; Janek, J.; Manke, I.; Zeier, W. G.; Ohno, S. Visualizing Reaction Fronts and Transport Limitations in Solid-State Li-S Batteries via Operando Neutron Imaging. *Adv. Energy Mater.* **2023**, *13* (17), 2203426.
(49) Chen, C.; Oudenhoven, J. F. M.; Danilov, D. L.; Vezhlev, E.; Gao, L.; Li, N.; Mulder, F. M.; Eichel, R.-A.; Notten, P. H. L. Origin of Degradation in Si-Based All-Solid-State Li-Ion Microbatteries. *Adv. Energy Mater.* **2018**, *8* (30), 1801430.
(50) Cao, D.; Zhang, Y.; Ji, T.; Zhao, X.; Cakmak, E.; Ozcan, S.; Geiwitz, M.; Bilheux, J.; Xu, K.; Wang, Y.; et al. Li Dynamics in Mixed Ionic-Electronic Conducting Interlayer of All-Solid-State Li-Metal Batteries. *Nano Lett.* **2024**, *24* (5), 1544−1552.
(51) Cao, D.; Zhang, K.; Li, W.; Zhang, Y.; Ji, T.; Zhao, X.; Cakmak, E.; Zhu, J.; Cao, Y.; Zhu, H. Nondestructively Visualizing and Understanding the Mechano-Electro-Chemical Origins of "Soft Short" and "Creeping" in All-Solid-State Batteries. *Adv. Funct. Mater.* **2023**, *33* (52), 2307998.
(52) Zhong, Y.; Zhang, X.; Zhang, Y.; Jia, P.; Xi, Y.; Kang, L.; Yu, Z. Understanding and Unveiling the Electro-Chemo-Mechanical Behavior in Solid-State Batteries. *SusMat* **2024**, *4* (2), No. e190.
(53) Bradbury, R.; Kardjilov, N.; Dewald, G. F.; Tengattini, A.; Helfen, L.; Zeier, W. G.; Manke, I. Visualizing Lithium Ion Transport in Solid-

State Li-S Batteries Using ^{6}Li Contrast Enhanced Neutron Imaging. *Adv. Funct. Mater.* **2023**, *33* (38), 2302619.
(54) Zhang, X.; Zhang, S.; Lu, J.; Tang, F.; Dong, K.; Yu, Z.; Hilger, A.; Osenberg, M.; Markötter, H.; Wilde, F.; et al. Unveiling the Electro-Chemo-Mechanical Failure Mechanism of Sodium Metal Anodes in Sodium-Oxygen Batteries by Synchrotron X-Ray Computed Tomography. *Adv. Funct. Mater.* **2024**, *34*, 2402253.
(55) Cao, C.; Toney, M. F.; Sham, T.-K.; Harder, R.; Shearing, P. R.; Xiao, X.; Wang, J. Emerging X-Ray Imaging Technologies for Energy Materials. *Mater. Today* **2020**, *34*, 132−147.
(56) Lou, S.; Sun, N.; Zhang, F.; Liu, Q.; Wang, J. Tracking Battery Dynamics by Operando Synchrotron X-Ray Imaging: Operation from Liquid Electrolytes to Solid-State Electrolytes. *Acc. Mater. Res.* **2021**, *2* (12), 1177−1189.
(57) Lewis, J. A.; Cortes, F. J. Q.; Liu, Y.; Miers, J. C.; Verma, A.; Vishnugopi, B. S.; Tippens, J.; Prakash, D.; Marchese, T. S.; Han, S. Y.; et al. Linking Void and Interphase Evolution to Electrochemistry in Solid-State Batteries Using Operando X-Ray Tomography. *Nat. Mater.* **2021**, *20* (4), 503−510.
(58) Krauskopf, T.; Richter, F. H.; Zeier, W. G.; Janek, J. Physicochemical Concepts of the Lithium Metal Anode in Solid-State Batteries. *Chem. Rev.* **2020**, *120* (15), 7745−7794.
(59) Zekoll, S. Tuning the Properties of Ceramic Solid Electrolytes for Lithium Batteries. University of Oxford, 2018.
(60) Jackman, S. D.; Cutler, R. A. Effect of Microcracking on Ionic Conductivity in Latp. *J. Power Sources* **2012**, *218*, 65−72.
(61) Yu, S.; Schmidt, R. D.; Garcia-Mendez, R.; Herbert, E.; Dudney, N. J.; Wolfenstine, J. B.; Sakamoto, J.; Siegel, D. J. Elastic Properties of the Solid Electrolyte $Li_7La_3Zr_2O_{12}$ (LLZO). *Chem. Mater.* **2016**, *28* (1), 197−206.
(62) Guo, H.; Su, J.; Zha, W.; Xiu, T.; Song, Z.; Badding, M. E.; Jin, J.; Wen, Z. Achieving High Critical Current Density in Ta-Doped $Li_7La_3Zr_2O_{12}$/MgO Composite Electrolytes. *J. Alloys Compd.* **2021**, *856*, 157222.
(63) Kim, Y.; Jo, H.; Allen, J. L.; Choe, H.; Wolfenstine, J.; Sakamoto, J. The Effect of Relative Density on the Mechanical Properties of Hot-Pressed Cubic $Li_7La_3Zr_2O_{12}$. *J. Am. Ceram. Soc.* **2016**, *99* (4), 1367−1374.
(64) Cho, Y.-H.; Wolfenstine, J.; Rangasamy, E.; Kim, H.; Choe, H.; Sakamoto, J. Mechanical Properties of the Solid Li-Ion Conducting Electrolyte: $Li_{0.33}La_{0.57}TiO_3$. *J. Mater. Sci.* **2012**, *47* (16), 5970−5977.
(65) Deng, Z.; Wang, Z.; Chu, I.-H.; Luo, J.; Ong, S. P. Elastic Properties of Alkali Superionic Conductor Electrolytes from First Principles Calculations. *J. Electrochem. Soc.* **2016**, *163* (2), A67.
(66) Wang, Z. Q.; Wu, M. S.; Liu, G.; Lei, X. L.; Xu, B.; Ouyang, C. Y. Elastic Properties of New Solid State Electrolyte Material $Li_{10}GeP_2S_{12}$: A Study from First-Principles Calculations. *Int. J. Electrochem. Sci.* **2014**, *9* (2), 562−568.
(67) Herbert, E. G.; Tenhaeff, W. E.; Dudney, N. J.; Pharr, G. M. Mechanical Characterization of Lipon Films Using Nanoindentation. *Thin Solid Films* **2011**, *520* (1), 413−418.
(68) Sakuda, A.; Hayashi, A.; Takigawa, Y.; Higashi, K.; Tatsumisago, M. Evaluation of Elastic Modulus of Li_2S-P_2S_5 Glassy Solid Electrolyte by Ultrasonic Sound Velocity Measurement and Compression Test. *J. Ceram. Soc. Jpn.* **2013**, *121*, 946−949.
(69) Liu, H.; Cheng, X.-B.; Huang, J.-Q.; Yuan, H.; Lu, Y.; Yan, C.; Zhu, G.-L.; Xu, R.; Zhao, C.-Z.; Hou, L.-P.; et al. Controlling Dendrite Growth in Solid-State Electrolytes. *ACS Energy Lett.* **2020**, *5* (3), 833−843.
(70) Barai, P.; Higa, K.; Srinivasan, V. Effect of Initial State of Lithium on the Propensity for Dendrite Formation: A Theoretical Study. *J. Electrochem. Soc.* **2017**, *164* (2), A180.
(71) Monroe, C.; Newman, J. The Impact of Elastic Deformation on Deposition Kinetics at Lithium/Polymer Interfaces. *J. Electrochem. Soc.* **2005**, *152* (2), A396.
(72) Banerjee, A.; Wang, X.; Fang, C.; Wu, E. A.; Meng, Y. S. Interfaces and Interphases in All-Solid-State Batteries with Inorganic Solid Electrolytes. *Chem. Rev.* **2020**, *120* (14), 6878−6933.
(73) Dixit, M. B.; Singh, N.; Horwath, J. P.; Shevchenko, P. D.; Jones, M.; Stach, E. A.; Arthur, T. S.; Hatzell, K. B. In Situ Investigation of Chemomechanical Effects in Thiophosphate Solid Electrolytes. *Matter* **2020**, *3* (6), 2138−2159.
(74) Shen, F.; Dixit, M. B.; Xiao, X.; Hatzell, K. B. Effect of Pore Connectivity on Li Dendrite Propagation within LLZO Electrolytes Observed with Synchrotron X-Ray Tomography. *ACS Energy Lett.* **2018**, *3* (4), 1056−1061.
(75) Dixit, M. B.; Regala, M.; Shen, F.; Xiao, X.; Hatzell, K. B. Tortuosity Effects in Garnet-Type $Li_7La_3Zr_2O_{12}$ Solid Electrolytes. *ACS Appl. Mater. Interfaces* **2019**, *11* (2), 2022−2030.
(76) Hao, S.; Bailey, J. J.; Iacoviello, F.; Bu, J.; Grant, P. S.; Brett, D. J. L.; Shearing, P. R. 3D Imaging of Lithium Protrusions in Solid-State Lithium Batteries Using X-Ray Computed Tomography. *Adv. Funct. Mater.* **2021**, *31* (10), 2007564.
(77) Hao, S.; Daemi, S. R.; Heenan, T. M. M.; Du, W.; Tan, C.; Storm, M.; Rau, C.; Brett, D. J. L.; Shearing, P. R. Tracking Lithium Penetration in Solid Electrolytes in 3d by in-Situ Synchrotron X-Ray Computed Tomography. *Nano Energy* **2021**, *82*, 105744.
(78) Hu, B.; Zhang, S.; Ning, Z.; Spencer-Jolly, D.; Melvin, D. L. R.; Gao, X.; Perera, J.; Pu, S. D.; Rees, G. J.; Wang, L.; et al. Deflecting Lithium Dendritic Cracks in Multi-Layered Solid Electrolytes. *Joule* **2024**, *8*, 2623−2638.
(79) Madsen, K. E.; Bassett, K. L.; Ta, K.; Sforzo, B. A.; Matusik, K. E.; Kastengren, A. L.; Gewirth, A. A. Direct Observation of Interfacial Mechanical Failure in Thiophosphate Solid Electrolytes with Operando X-Ray Tomography. *Adv. Mater. Interfaces* **2020**, *7* (19), 2000751.
(80) Tippens, J.; Miers, J. C.; Afshar, A.; Lewis, J. A.; Cortes, F. J. Q.; Qiao, H.; Marchese, T. S.; Di Leo, C. V.; Saldana, C.; McDowell, M. T. Visualizing Chemomechanical Degradation of a Solid-State Battery Electrolyte. *ACS Energy Lett.* **2019**, *4* (6), 1475−1483.
(81) Sun, F.; Wang, C.; Osenberg, M.; Dong, K.; Zhang, S.; Yang, C.; Wang, Y.; Hilger, A.; Zhang, J.; Dong, S.; et al. Clarifying the Electro-Chemo-Mechanical Coupling in $Li_{10}SnP_2S_{12}$ Based All-Solid-State Batteries. *Adv. Energy Mater.* **2022**, *12* (13), 2103714.
(82) Harry, K. J.; Hallinan, D. T.; Parkinson, D. Y.; MacDowell, A. A.; Balsara, N. P. Detection of Subsurface Structures Underneath Dendrites Formed on Cycled Lithium Metal Electrodes. *Nat. Mater.* **2014**, *13* (1), 69−73.
(83) Ning, Z.; Jolly, D. S.; Li, G.; De Meyere, R.; Pu, S. D.; Chen, Y.; Kasemchainan, J.; Ihli, J.; Gong, C.; Liu, B.; et al. Visualizing Plating-Induced Cracking in Lithium-Anode Solid-Electrolyte Cells. *Nat. Mater.* **2021**, *20* (8), 1121−1129.
(84) Ning, Z.; Li, G.; Melvin, D. L. R.; Chen, Y.; Bu, J.; Spencer-Jolly, D.; Liu, J.; Hu, B.; Gao, X.; Perera, J.; et al. Dendrite Initiation and Propagation in Lithium Metal Solid-State Batteries. *Nature* **2023**, *618* (7964), 287−293.
(85) Cheng, E. J.; Sharafi, A.; Sakamoto, J. Intergranular Li Metal Propagation through Polycrystalline $Li_{6.25}Al_{0.25}La_3Zr_2O_{12}$ Ceramic Electrolyte. *Electrochim. Acta* **2017**, *223*, 85−91.
(86) Lin, F.; Liu, Y.; Yu, X.; Cheng, L.; Singer, A.; Shpyrko, O. G.; Xin, H. L.; Tamura, N.; Tian, C.; Weng, T.-C.; et al. Synchrotron X-Ray Analytical Techniques for Studying Materials Electrochemistry in Rechargeable Batteries. *Chem. Rev.* **2017**, *117* (21), 13123−13186.
(87) Sun, F.; Dong, K.; Osenberg, M.; Hilger, A.; Risse, S.; Lu, Y.; Kamm, P. H.; Klaus, M.; Markötter, H.; García-Moreno, F.; et al. Visualizing the Morphological and Compositional Evolution of the Interface of Inli-AnodelThio-Lision Electrolyte in an All-Solid-State Li-S Cell by in Operando Synchrotron X-Ray Tomography and Energy Dispersive Diffraction. *J. Mater. Chem. A* **2018**, *6* (45), 22489−22496.
(88) Augustyn, V.; McDowell, M. T.; Vojvodic, A. Toward an Atomistic Understanding of Solid-State Electrochemical Interfaces for Energy Storage. *Joule* **2018**, *2* (11), 2189−2193.
(89) Wenzel, S.; Leichtweiss, T.; Krüger, D.; Sann, J.; Janek, J. Interphase Formation on Lithium Solid Electrolytes—an in Situ Approach to Study Interfacial Reactions by Photoelectron Spectroscopy. *Solid State Ion.* **2015**, *278*, 98−105.
(90) Lewis, J. A.; Cortes, F. J. Q.; Boebinger, M. G.; Tippens, J.; Marchese, T. S.; Kondekar, N.; Liu, X.; Chi, M.; McDowell, M. T.

Interphase Morphology between a Solid-State Electrolyte and Lithium Controls Cell Failure. *ACS Energy Lett.* **2019**, *4* (2), 591−599.
(91) Otoyama, M.; Suyama, M.; Hotehama, C.; Kowada, H.; Takeda, Y.; Ito, K.; Sakuda, A.; Tatsumisago, M.; Hayashi, A. Visualization and Control of Chemically Induced Crack Formation in All-Solid-State Lithium-Metal Batteries with Sulfide Electrolyte. *ACS Appl. Mater. Interfaces* **2021**, *13* (4), 5000−5007.
(92) Doux, J.-M.; Nguyen, H.; Tan, D. H. S.; Banerjee, A.; Wang, X.; Wu, E. A.; Jo, C.; Yang, H.; Meng, Y. S. Stack Pressure Considerations for Room-Temperature All-Solid-State Lithium Metal Batteries. *Adv. Energy Mater.* **2020**, *10* (1), 1903253.
(93) Lewis, J. A.; Tippens, J.; Cortes, F. J. Q.; McDowell, M. T. Chemo-Mechanical Challenges in Solid-State Batteries. *Trends Chem.* **2019**, *1* (9), 845−857.
(94) Xiao, Y.; Wang, Y.; Bo, S.-H.; Kim, J. C.; Miara, L. J.; Ceder, G. Understanding Interface Stability in Solid-State Batteries. *Nat. Rev. Mater.* **2020**, *5* (2), 105−126.
(95) de Vasconcelos, L. S.; Xu, R.; Xu, Z.; Zhang, J.; Sharma, N.; Shah, S. R.; Han, J.; He, X.; Wu, X.; Sun, H.; et al. Chemomechanics of Rechargeable Batteries: Status, Theories, and Perspectives. *Chem. Rev.* **2022**, *122* (15), 13043−13107.
(96) Koerver, R.; Zhang, W.; de Biasi, L.; Schweidler, S.; Kondrakov, A. O.; Kolling, S.; Brezesinski, T.; Hartmann, P.; Zeier, W. G.; Janek, J. Chemo-Mechanical Expansion of Lithium Electrode Materials - on the Route to Mechanically Optimized All-Solid-State Batteries. *Energy Environ. Sci.* **2018**, *11* (8), 2142−2158.
(97) Manalastas, W.; Rikarte, J.; Chater, R. J.; Brugge, R.; Aguadero, A.; Buannic, L.; Llordés, A.; Aguesse, F.; Kilner, J. Mechanical Failure of Garnet Electrolytes During Li Electrodeposition Observed by in-Operando Microscopy. *J. Power Sources* **2019**, *412*, 287−293.
(98) Kasemchainan, J.; Zekoll, S.; Spencer Jolly, D.; Ning, Z.; Hartley, G. O.; Marrow, J.; Bruce, P. G. Critical Stripping Current Leads to Dendrite Formation on Plating in Lithium Anode Solid Electrolyte Cells. *Nat. Mater.* **2019**, *18* (10), 1105−1111.
(99) Wang, M. J.; Choudhury, R.; Sakamoto, J. Characterizing the Li-Solid-Electrolyte Interface Dynamics as a Function of Stack Pressure and Current Density. *Joule* **2019**, *3* (9), 2165−2178.
(100) Hänsel, C.; Kundu, D. The Stack Pressure Dilemma in Sulfide Electrolyte Based Li Metal Solid-State Batteries: A Case Study with Li6psScl Solid Electrolyte. *Adv. Mater. Interfaces* **2021**, *8* (10), 2100206.
(101) Lee, C.; Han, S. Y.; Lewis, J. A.; Shetty, P. P.; Yeh, D.; Liu, Y.; Klein, E.; Lee, H.-W.; McDowell, M. T. Stack Pressure Measurements to Probe the Evolution of the Lithium-Solid-State Electrolyte Interface. *ACS Energy Lett.* **2021**, *6* (9), 3261−3269.
(102) Masias, A.; Felten, N.; Garcia-Mendez, R.; Wolfenstine, J.; Sakamoto, J. Elastic, Plastic, and Creep Mechanical Properties of Lithium Metal. *J. Mater. Sci.* **2019**, *54* (3), 2585−2600.
(103) LePage, W. S.; Chen, Y.; Kazyak, E.; Chen, K.-H.; Sanchez, A. J.; Poli, A.; Arruda, E. M.; Thouless, M. D.; Dasgupta, N. P. Lithium Mechanics: Roles of Strain Rate and Temperature and Implications for Lithium Metal Batteries. *J. Electrochem. Soc.* **2019**, *166* (2), A89−A97.
(104) Zhang, W.; Schröder, D.; Arlt, T.; Manke, I.; Koerver, R.; Pinedo, R.; Weber, D. A.; Sann, J.; Zeier, W. G.; Janek, J. (Electro)Chemical Expansion During Cycling: Monitoring the Pressure Changes in Operating Solid-State Lithium Batteries. *J. Mater. Chem. A* **2017**, *5* (20), 9929−9936.
(105) Schreiber, A.; Rosen, M.; Waetzig, K.; Nikolowski, K.; Schiffmann, N.; Wiggers, H.; KüPers, M.; Fattakhova-Rohlfing, D.; Kuckshinrichs, W.; Guillon, O.; Finsterbusch, M. Oxide Ceramic Electrolytes for All-Solid-State Lithium Batteries - Cost-Cutting Cell Design and Environmental Impact. *Green Chem.* **2023**, *25* (1), 399−414.
(106) Sakamoto, J. More Pressure Needed. *Nat. Energy* **2019**, *4* (10), 827−828.
(107) Zhang, X.; Wang, Q. J.; Harrison, K. L.; Roberts, S. A.; Harris, S. J. Pressure-Driven Interface Evolution in Solid-State Lithium Metal Batteries. *Cell Rep. Phys. Sci.* **2020**, *1* (2), 100012.
(108) Barroso-Luque, L.; Tu, Q.; Ceder, G. An Analysis of Solid-State Electrodeposition-Induced Metal Plastic Flow and Predictions of Stress States in Solid Ionic Conductor Defects. *J. Electrochem. Soc.* **2020**, *167* (2), 020534.
(109) Liang, Y.; Liu, H.; Wang, G.; Wang, C.; Ni, Y.; Nan, C.-W.; Fan, L.-Z. Challenges, Interface Engineering, and Processing Strategies toward Practical Sulfide-Based All-Solid-State Lithium Batteries. *InfoMat* **2022**, *4* (5), No. e12292.
(110) He, Y.; Lu, C.; Liu, S.; Zheng, W.; Luo, J. Interfacial Incompatibility and Internal Stresses in All-Solid-State Lithium Ion Batteries. *Adv. Energy Mater.* **2019**, *9* (36), 1901810.
(111) Wang, M. J.; Kazyak, E.; Dasgupta, N. P.; Sakamoto, J. Transitioning Solid-State Batteries from Lab to Market: Linking Electro-Chemo-Mechanics with Practical Considerations. *Joule* **2021**, *5* (6), 1371−1390.
(112) Sun, S.; Zhao, C.-Z.; Yuan, H.; Lu, Y.; Hu, J.-K.; Huang, J.-Q.; Zhang, Q. Cathode Multiscale Understanding of High-Energy Cathodes in Solid-State Batteries: From Atomic Scale to Macroscopic Scale. *Mater. Futures* **2022**, *1* (1), 012101.
(113) McGrogan, F. P.; Swamy, T.; Bishop, S. R.; Eggleton, E.; Porz, L.; Chen, X.; Chiang, Y.-M.; Van Vliet, K. J. Compliant yet Brittle Mechanical Behavior of Li_2S-P_2S_5 Lithium-Ion-Conducting Solid Electrolyte. *Adv. Energy Mater.* **2017**, *7* (12), 1602011.
(114) Neumann, A.; Randau, S.; Becker-Steinberger, K.; Danner, T.; Hein, S.; Ning, Z.; Marrow, J.; Richter, F. H.; Janek, J.; Latz, A. Analysis of Interfacial Effects in All-Solid-State Batteries with Thiophosphate Solid Electrolytes. *ACS Appl. Mater. Interfaces* **2020**, *12* (8), 9277−9291.
(115) Reimers, J. N.; Dahn, J. R. Electrochemical and in Situ X-Ray Diffraction Studies of Lithium Intercalation in Li_xCoO_2. *J. Electrochem. Soc.* **1992**, *139* (8), 2091.
(116) Bucci, G.; Christensen, J. Modeling of Lithium Electro-deposition at the Lithium/Ceramic Electrolyte Interface: The Role of Interfacial Resistance and Surface Defects. *J. Power Sources* **2019**, *441*, 227186.
(117) Bucci, G.; Swamy, T.; Bishop, S.; Sheldon, B. W.; Chiang, Y.-M.; Carter, W. C. The Effect of Stress on Battery-Electrode Capacity. *J. Electrochem. Soc.* **2017**, *164* (4), A645.
(118) Bucci, G.; Talamini, B.; Renuka Balakrishna, A.; Chiang, Y.-M.; Carter, W. C. Mechanical Instability of Electrode-Electrolyte Interfaces in Solid-State Batteries. *Phys. Rev. Mater.* **2018**, *2* (10), 105407.
(119) Koerver, R.; Aygün, I.; Leichtweiß, T.; Dietrich, C.; Zhang, W.; Binder, J. O.; Hartmann, P.; Zeier, W. G.; Janek, J. Capacity Fade in Solid-State Batteries: Interphase Formation and Chemomechanical Processes in Nickel-Rich Layered Oxide Cathodes and Lithium Thiophosphate Solid Electrolytes. *Chem. Mater.* **2017**, *29* (13), 5574−5582.
(120) Zou, J.; Wu, Z.; Tang, R.; Ren, Z.; Niu, X.; Wang, L. Copper Diffusion Related Phase Change and Voltage Decay in Cus Cathode. *Nano Res.* **2023**, *16* (6), 8497−8503.
(121) Jiang, K.; Chen, Z.; Meng, X. Cus and Cu2s as Cathode Materials for Lithium Batteries: A Review. *ChemElectroChem.* **2019**, *6* (11), 2825−2840.
(122) Hosseini, S. M.; Varzi, A.; Ito, S.; Aihara, Y.; Passerini, S. High Loading CuS-Based Cathodes for All-Solid-State Lithium Sulfur Batteries with Enhanced Volumetric Capacity. *Energy Storage Mater.* **2020**, *27*, 61−68.
(123) Zhao, J.; Tang, Y.; Dai, Q.; Du, C.; Zhang, Y.; Xue, D.; Chen, T.; Chen, J.; Wang, B.; Yao, J.; et al. In Situ Observation of Li Deposition-Induced Cracking in Garnet Solid Electrolytes. *Energy Environ. Mater.* **2022**, *5* (2), 524−532.
(124) Kinzer, B.; Davis, A. L.; Krauskopf, T.; Hartmann, H.; LePage, W. S.; Kazyak, E.; Janek, J.; Dasgupta, N. P.; Sakamoto, J. Operando Analysis of the Molten Li|LLZO Interface: Understanding How the Physical Properties of Li Affect the Critical Current Density. *Matter* **2021**, *4* (6), 1947−1961.
(125) Kazyak, E.; Garcia-Mendez, R.; LePage, W. S.; Sharafi, A.; Davis, A. L.; Sanchez, A. J.; Chen, K.-H.; Haslam, C.; Sakamoto, J.; Dasgupta, N. P. Li Penetration in Ceramic Solid Electrolytes: Operando Microscopy Analysis of Morphology, Propagation, and Reversibility. *Matter* **2020**, *2* (4), 1025−1048.

https://doi.org/10.1021/acsenergylett.4c02476
ACS Energy Lett. 2025, 10, 496−525

(126) Han, S. Y.; Lewis, J. A.; Shetty, P. P.; Tippens, J.; Yeh, D.; Marchese, T. S.; McDowell, M. T. Porous Metals from Chemical Dealloying for Solid-State Battery Anodes. *Chem. Mater.* **2020**, *32* (6), 2461−2469.
(127) Yu, Z.; Zhang, X.; Fu, C.; Wang, H.; Chen, M.; Yin, G.; Huo, H.; Wang, J. Dendrites in Solid-State Batteries: Ion Transport Behavior, Advanced Characterization, and Interface Regulation. *Adv. Energy Mater.* **2021**, *11* (18), 2003250.
(128) Siniscalchi, M.; Shi, Y.; Li, G.; Gibson, J. S.; Weatherup, R. S.; Bonilla, R. S.; Speller, S. C.; Grovenor, C. R. M. Initiation of Dendritic Failure of LLZTO via Sub-Surface Lithium Deposition. *Energy Environ. Sci.* **2024**, *17* (7), 2431−2440.
(129) Cao, T.; Xu, R.; Cheng, X.; Wang, M.; Sun, T.; Lu, J.; Liu, X.; Zhang, Y.; Zhang, Z. Chemomechanical Origins of the Dynamic Evolution of Isolated Li Filaments in Inorganic Solid-State Electrolytes. *Nano Lett.* **2024**, *24* (6), 1843−1850.
(130) Diallo, M. S.; Shi, T.; Zhang, Y.; Peng, X.; Shozib, I.; Wang, Y.; Miara, L. J.; Scott, M. C.; Tu, Q. H.; Ceder, G. Effect of Solid-Electrolyte Pellet Density on Failure of Solid-State Batteries. *Nat. Commun.* **2024**, *15* (1), 858.
(131) Gao, J.; Zhu, J.; Li, X.; Li, J.; Guo, X.; Li, H.; Zhou, W. Rational Design of Mixed Electronic-Ionic Conducting Ti-Doping $Li_7La_3Zr_2O_{12}$ for Lithium Dendrites Suppression. *Adv. Funct. Mater.* **2021**, *31* (2), 2001918.
(132) Tu, Q.; Shi, T.; Chakravarthy, S.; Ceder, G. Understanding Metal Propagation in Solid Electrolytes Due to Mixed Ionic-Electronic Conduction. *Matter* **2021**, *4* (10), 3248−3268.
(133) Sun, M.; Liu, T.; Yuan, Y.; Ling, M.; Xu, N.; Liu, Y.; Yan, L.; Li, H.; Liu, C.; Lu, Y.; et al. Visualizing Lithium Dendrite Formation within Solid-State Electrolytes. *ACS Energy Lett.* **2021**, *6* (2), 451−458.
(134) Choi, S.; Jeon, M.; Ahn, J.; Jung, W. D.; Choi, S. M.; Kim, J.-S.; Lim, J.; Jang, Y.-J.; Jung, H.-G.; Lee, J.-H.; et al. Quantitative Analysis of Microstructures and Reaction Interfaces on Composite Cathodes in All-Solid-State Batteries Using a Three-Dimensional Reconstruction Technique. *ACS Appl. Mater. Interfaces* **2018**, *10* (28), 23740−23747.
(135) Kroll, M.; Duchardt, M.; Karstens, S. L.; Schlabach, S.; Lange, F.; Hochstrasser, J.; Roling, B.; Tallarek, U. Sheet-Type All-Solid-State Batteries with Sulfidic Electrolytes: Analysis of Kinetic Limitations Based on a Cathode Morphology Study. *J. Power Sources* **2021**, *505*, 230064.
(136) Hlushkou, D.; Reising, A. E.; Kaiser, N.; Spannenberger, S.; Schlabach, S.; Kato, Y.; Roling, B.; Tallarek, U. The Influence of Void Space on Ion Transport in a Composite Cathode for All-Solid-State Batteries. *J. Power Sources* **2018**, *396*, 363−370.
(137) Nakamura, H.; Kawaguchi, T.; Masuyama, T.; Sakuda, A.; Saito, T.; Kuratani, K.; Ohsaki, S.; Watano, S. Dry Coating of Active Material Particles with Sulfide Solid Electrolytes for an All-Solid-State Lithium Battery. *J. Power Sources* **2020**, *448*, 227579.
(138) Zhang, C.; Feng, Y.; Han, Z.; Gao, S.; Wang, M.; Wang, P. Electrochemical and Structural Analysis in All-Solid-State Lithium Batteries by Analytical Electron Microscopy: Progress and Perspectives. *Adv. Mater.* **2020**, *32* (27), 1903747.
(139) Cheng, D.; Wynn, T. A.; Wang, X.; Wang, S.; Zhang, M.; Shimizu, R.; Bai, S.; Nguyen, H.; Fang, C.; Kim, M.-c.; et al. Unveiling the Stable Nature of the Solid Electrolyte Interphase between Lithium Metal and Lipon Via Cryogenic Electron Microscopy. *Joule* **2020**, *4* (11), 2484−2500.
(140) Weng, S.; Li, Y.; Wang, X. Cryo-EM for Battery Materials and Interfaces: Workflow, Achievements, and Perspectives. *iScience* **2021**, *24* (12), 103402.
(141) Peled, E.; Golodnitsky, D.; Ardel, G.; Eshkenazy, V. The Sei Model—Application to Lithium-Polymer Electrolyte Batteries. *Electrochim. Acta* **1995**, *40* (13−14), 2197−2204.
(142) Wang, A.; Kadam, S.; Li, H.; Shi, S.; Qi, Y. Review on Modeling of the Anode Solid Electrolyte Interphase (SEI) for Lithium-Ion Batteries. *Npj Comput. Mater.* **2018**, *4* (1), 15.
(143) Wang, C.; Meng, Y. S.; Xu, K. Perspective—Fluorinating Interphases. *J. Electrochem. Soc.* **2019**, *166* (3), A5184.
(144) Peled, E. The Electrochemical Behavior of Alkali and Alkaline Earth Metals in Nonaqueous Battery Systems—the Solid Electrolyte Interphase Model. *J. Electrochem. Soc.* **1979**, *126* (12), 2047.
(145) Aurbach, D.; Ein-Ely, Y.; Zaban, A. The Surface Chemistry of Lithium Electrodes in Alkyl Carbonate Solutions. *J. Electrochem. Soc.* **1994**, *141* (1), L1.
(146) Ma, C.; Cheng, Y.; Yin, K.; Luo, J.; Sharafi, A.; Sakamoto, J.; Li, J.; More, K. L.; Dudney, N. J.; Chi, M. Interfacial Stability of Li Metal-Solid Electrolyte Elucidated Via in Situ Electron Microscopy. *Nano Lett.* **2016**, *16* (11), 7030−7036.
(147) Weiss, M.; Seidlhofer, B.-K.; Geiß, M.; Geis, C.; Busche, M. R.; Becker, M.; Vargas-Barbosa, N. M.; Silvi, L.; Zeier, W. G.; Schröder, D.; Janek, J. Unraveling the Formation Mechanism of Solid-Liquid Electrolyte Interphases on LIPON Thin Films. *ACS Appl. Mater. Interfaces* **2019**, *11* (9), 9539−9547.
(148) Wood, K. N.; Steirer, K. X.; Hafner, S. E.; Ban, C.; Santhanagopalan, S.; Lee, S.-H.; Teeter, G. Operando X-Ray Photoelectron Spectroscopy of Solid Electrolyte Interphase Formation and Evolution in Li_2S-P_2S_5 Solid-State Electrolytes. *Nat. Commun.* **2018**, *9* (1), 2490.
(149) Zhu, Y.; He, X.; Mo, Y. Origin of Outstanding Stability in the Lithium Solid Electrolyte Materials: Insights from Thermodynamic Analyses Based on First-Principles Calculations. *ACS Appl. Mater. Interfaces* **2015**, *7* (42), 23685−23693.
(150) Shimizu, R.; Cheng, D.; Weaver, J. L.; Zhang, M.; Lu, B.; Wynn, T. A.; Burger, R.; Kim, M.-c.; Zhu, G.; Meng, Y. S. Unraveling the Stable Cathode Electrolyte Interface in All Solid-State Thin-Film Battery Operating at 5 V. *Adv. Energy Mater.* **2022**, *12* (31), 2201119.
(151) Ebadi, M.; Costa, L. T.; Araujo, C. M.; Brandell, D. Modelling the Polymer Electrolyte/Li-Metal Interface by Molecular Dynamics Simulations. *Electrochim. Acta* **2017**, *234*, 43−51.
(152) Mirsakiyeva, A.; Ebadi, M.; Araujo, C. M.; Brandell, D.; Broqvist, P.; Kullgren, J. Initial Steps in Peo Decomposition on a Li Metal Electrode. *J. Phys. Chem. C* **2019**, *123* (37), 22851−22857.
(153) Sheng, O.; Jin, C.; Chen, M.; Ju, Z.; Liu, Y.; Wang, Y.; Nai, J.; Liu, T.; Zhang, W.; Tao, X. Platinum Nano-Interlayer Enhanced Interface for Stable All-Solid-State Batteries Observed Via Cryo-Transmission Electron Microscopy. *J. Mater. Chem. A* **2020**, *8* (27), 13541−13547.
(154) Sheng, O.; Zheng, J.; Ju, Z.; Jin, C.; Wang, Y.; Chen, M.; Nai, J.; Liu, T.; Zhang, W.; Liu, Y.; Tao, X. In Situ Construction of a Lif-Enriched Interface for Stable All-Solid-State Batteries and Its Origin Revealed by Cryo-TEM. *Adv. Mater.* **2020**, *32* (34), 2000223.
(155) Okita, K.; Ikeda, K.-i.; Sano, H.; Iriyama, Y.; Sakaebe, H. Stabilizing Lithium Plating-Stripping Reaction between a Lithium Phosphorus Oxynitride Glass Electrolyte and Copper Thin Film by Platinum Insertion. *J. Power Sources* **2011**, *196* (4), 2135−2142.
(156) Yan, K.; Lu, Z.; Lee, H.-W.; Xiong, F.; Hsu, P.-C.; Li, Y.; Zhao, J.; Chu, S.; Cui, Y. Selective Deposition and Stable Encapsulation of Lithium through Heterogeneous Seeded Growth. *Nat. Energy* **2016**, *1* (3), 1−8.
(157) Dai, Q.; Yao, J.; Du, C.; Ye, H.; Gao, Z.; Zhao, J.; Chen, J.; Su, Y.; Li, H.; Fu, X.; et al. Cryo-Em Studies of Atomic-Scale Structures of Interfaces in Garnet-Type Electrolyte Based Solid-State Batteries. *Adv. Funct. Mater.* **2022**, *32* (51), 2208682.
(158) Sheng, O.; Jin, C.; Ju, Z.; Zheng, J.; Liu, T.; Liu, Y.; Wang, Y.; Luo, J.; Tao, X.; Nai, J. Stabilizing Li4sns4 Electrolyte from Interface to Bulk Phase with a Gradient Lithium Iodide/Polymer Layer in Lithium Metal Batteries. *Nano Lett.* **2022**, *22* (20), 8346−8354.
(159) Qian, G.; Zhang, J.; Chu, S.-Q.; Li, J.; Zhang, K.; Yuan, Q.; Ma, Z.-F.; Pianetta, P.; Li, L.; Jung, K.; Liu, Y. Understanding the Mesoscale Degradation in Nickel-Rich Cathode Materials through Machine-Learning-Revealed Strain-Redox Decoupling. *ACS Energy Lett.* **2021**, *6* (2), 687−693.
(160) Zhang, K.; Ren, F.; Wang, X.; Hu, E.; Xu, Y.; Yang, X.-Q.; Li, H.; Chen, L.; Pianetta, P.; Mehta, A.; et al. Finding a Needle in the Haystack: Identification of Functionally Important Minority Phases in an Operating Battery. *Nano Lett.* **2017**, *17* (12), 7782−7788.

(161) Huang, Y.; Perlmutter, D.; Fei-Huei Su, A.; Quenum, J.; Shevchenko, P.; Parkinson, D. Y.; Zenyuk, I. V.; Ushizima, D. Detecting Lithium Plating Dynamics in a Solid-State Battery with Operando X-Ray Computed Tomography Using Machine Learning. *Npj Comput. Mater.* **2023**, *9* (1), 93.
(162) Su, B.; Li, J.; Deng, B.; Pianetta, P.; Liu, Y. Multi-Modal X-Ray Microscopy for Chemical Analysis. *TrAC-Trend Anal. Chem.* **2024**, *171*, 117491.
(163) Müller, S.; Sauter, C.; Shunmugasundaram, R.; Wenzler, N.; De Andrade, V.; De Carlo, F.; Konukoglu, E.; Wood, V. Deep Learning-Based Segmentation of Lithium-Ion Battery Microstructures Enhanced by Artificially Generated Electrodes. *Nat. Commun.* **2021**, *12* (1), 6205.
(164) Ning, Y.; Yang, F.; Zhang, Y.; Qiang, Z.; Yin, G.; Wang, J.; Lou, S. Bridging Multimodal Data and Battery Science with Machine Learning. *Matter* **2024**, *7* (6), 2011−2032.
(165) Scharf, J.; Chouchane, M.; Finegan, D. P.; Lu, B.; Redquest, C.; Kim, M.-c.; Yao, W.; Franco, A. A.; Gostovic, D.; Liu, Z.; et al. Bridging Nano- and Microscale X-Ray Tomography for Battery Research by Leveraging Artificial Intelligence. *Nat. Nanotechnol.* **2022**, *17* (5), 446−459.
(166) Fu, T.; Zhang, K.; Wang, Y.; Li, J.; Zhang, J.; Yao, C.; He, Q.; Wang, S.; Huang, W.; Yuan, Q.; et al. Deep-Learning-Based Image Registration for Nano-Resolution Tomographic Reconstruction. *J. Synchrotron Radiat.* **2021**, *28* (6), 1909−1915.
(167) Ng, M.-F.; Zhao, J.; Yan, Q.; Conduit, G. J.; Seh, Z. W. Predicting the State of Charge and Health of Batteries Using Data-Driven Machine Learning. *Nat. Mach. Intell.* **2020**, *2* (3), 161−170.
(168) Lee, J. Z.; Wynn, T. A.; Schroeder, M. A.; Alvarado, J.; Wang, X.; Xu, K.; Meng, Y. S. Cryogenic Focused Ion Beam Characterization of Lithium Metal Anodes. *ACS Energy Lett.* **2019**, *4* (2), 489−493.
(169) Cheng, D.; Lu, B.; Raghavendran, G.; Zhang, M.; Meng, Y. S. Leveraging Cryogenic Electron Microscopy for Advancing Battery Design. *Matter* **2022**, *5* (1), 26−42.
(170) Yousaf, M.; Naseer, U.; Imran, A.; Li, Y.; Aftab, W.; Mahmood, A.; Mahmood, N.; Zhang, X.; Gao, P.; Lu, Y.; et al. Visualization of Battery Materials and Their Interfaces/Interphases Using Cryogenic Electron Microscopy. *Mater. Today* **2022**, *58*, 238−274.
(171) Zhang, L.; Fan, H.; Dang, Y.; Zhuang, Q.; Arandiyan, H.; Wang, Y.; Cheng, N.; Sun, H.; Pérez Garza, H. H.; Zheng, R.; et al. Recent Advances in in Situ and Operando Characterization Techniques for $Li_7La_3Zr_2O_{12}$-Based Solid-State Lithium Batteries. *Mater. Horiz.* **2023**, *10* (5), 1479−1538.

https://doi.org/10.1021/acsenergylett.4c02476
ACS Energy Lett. 2025, 10, 496−525